



# Estimating the Snow Density using Collocated Parsivel and MRR Measurements: A Preliminary Study from ICE-POP 2017/2018

Wei-Yu Chang<sup>1</sup>, Yung-Chuan Yang<sup>1</sup>, Chen-Yu Hung<sup>1</sup>, Kwonil Kim<sup>2</sup>, Gyuwon Lee<sup>3</sup>

<sup>1</sup>Department of Atmospheric Sciences, National Central University, Taoyuan, Taiwan

5 <sup>2</sup>School of Marine and Atmospheric Sciences, Stony Brook University, NY, USA

<sup>3</sup>Department of Atmospheric Sciences, Center for Atmospheric REmote sensing (CARE), Kyungpook National University, Daegu, Republic of Korea

Correspondence to: Wei-Yu Chang (wychang@g.ncu.edu.tw)

**Abstract.** A new method is developed to derive the hydrometer's bulk density and bulk water fraction from collocated measurements from Micro-Rain Radar (MRR) and Particle Size and Velocity disdrometer (Parsivel). Rigorous particle scattering simulation, namely the T-matrix method, is applied to particle size distribution data of Parsivel to calculate the reflectivity ( $Z_{HH}$ ). The possible combinations of the particle's ice, air, and water are derived to compare them with the MRR-measured  $Z_{HH}$ . The combination of minimum water fraction subsequently determines the bulk density ( $\rho_{bulk}$ ). The proposed method is applied to the data collected from the International Collaborative Experiments for Pyeongchang 2018 Olympic and Paralympic Winter Games (ICE-POP 2018) Projects and its pre-campaign. The estimated  $\rho_{bulk}$  was examined by self-evaluation of reflectivity weighted fall velocity ( $V_z$ ) of MRR and independent comparison of the liquid-equivalent snowfall rate (SR) of collocated Pluvio. The bias values are adequately low ( $V_z$ :  $-0.27\sim 0.14$  m s<sup>-1</sup>, SR:  $0.52\sim 0.74$  mm hr<sup>-1</sup>). The correlation coefficient of calculated SR from estimated  $\rho_{bulk}$  and observed SR from Pluvio can be up to 0.74. The results indicate the capability to derive reliable  $\rho_{bulk}$  through the proposed method, leveraging the compact and easily deployable designs of MRR and Parsivel. The derived bulk density of the two warm-low cases (28 February and 07 March 2018) shares a similar transition as the systems were decaying. The particles with higher bulk density and bulk water fraction were found in the coastal sites (BKC and GWU: mean  $\rho_{bulk}$  values are 0.12 to 0.25 g cm<sup>-3</sup>), typically accompanied by higher liquid-water constituents (mean values of the top 5% bulk water fraction are 0.33 to 0.50) than the inland sites (YPO and MHS: mean  $\rho_{bulk}$  values are 0.09 to 0.08 and mean values of the top 5% bulk water fraction are 0.001 to 0.029) during such synoptic conditions.

## 25 1 Introduction

The particle size distributions (PSD) and physical properties of hydrometers in winter storms are essential to discriminate among hydrometeor types (e.g., riming and aggregate snow) and develop algorithms (e.g., quantitative precipitation estimation of snow) for estimating the liquid water content of hydrometer with remote sensors (e.g., polarimetric radar and satellite). These physical properties, including terminal fall speed, shape, composition, and density, are crucial to verifying and improving microphysical parameterizations in numerical forecast models (Yuter et al. 2006; Kim et al. 2021). For example,



riming processes led to snowfall velocity and density diversity in the same particle diameter size (Zhang et al. 2021). The supercooled liquid water freezes on snow particles and fills in the holes of snow; therefore, snow's mass and fall velocity increase while size has little changes (Heymsfield 1982; Moisseev et al. 2018). On the other hand, the melting process induces higher fall velocity and density by increasing liquid phase fraction in a warm environment. The dispersed fall velocity caused by particles melted from dry snow to rain leads to higher collision efficiency and facilitates the aggregation and accretion processes (Yuter et al. 2006). Higher snow density is associated with steeper fall velocity and diameter (V-D) relations, which result from stronger riming (Lee et al. 2015) or melting processes (Yuter et al. 2006). To emulate the diverse physical properties of hydrometers, Morrison and Milbrandt (2015) proposed a new bulk method to parameterize ice-phase particles with evolvable density to study the role of density in numerical simulation. Radar-based quantitative precipitation estimation (QPE) of liquid equivalent snowfall rate (SR) from equivalent reflectivity ( $Z_e$ ) inhibits great uncertainty due to the diversity of snow properties (Huang et al. 2010, 2015, and 2019). Pre-assumed snow density in  $Z_e$ -SR relation is one of the critical factors. The snow density caused by various degrees of riming and melting processes is essential to derive the  $Z_e$ -SR relation (Huang et al. 2014).

As the snow density cannot be measured directly, various techniques with diverse measuring principles have been developed to investigate snow density using observational data. Brandes et al. (2007) estimated the bulk snow density from a two-dimensional video distrometer (2DVD) derived precipitation volume and the collocated gauge-measured precipitation mass. A climatological relation of bulk snow density and median volume diameter ( $D_0$ ) is also obtained. Nevertheless, various factors influence the density of frozen precipitation, which cannot be well illustrated by size-density relation (Roebber et al. 2003); Zhang and Luchs (2011) proposed a terminal velocity-based modification to the density value derived from the equation for terminal fall velocity (Pruppacher and Klett 1997). Several studies have proven that after the differentiation of riming degree, the density of snow can be derived correctly from the corresponding size (Li et al. 2018; Zhang et al. 2021; Lee et al. 2015; Zhang and Luchs 2011). An alternative approach is to use radar reflectivity to constrain the estimated bulk snow density. Huang et al. (2010) utilized a 2DVD to derive snow's particle size distribution (PSD) and a C-band dual-polarimetric radar to obtain the reflectivity on top of 2DVD. The measured reflectivity ( $Z_e$ ) was subsequently used to estimate the snow density by minimizing the measured  $Z_e$  from radar and calculated  $Z_e$  from 2DVD. Mroz et al. (2021) proposed an algorithm utilizing triple-frequency (X, Ka, W) radar measurements to retrieve the size, ice water content (IWC), and degree of riming of ice clouds. The results indicate the estimates of the mass-weighted diameters and IWC estimates are adequately accurate. Yet, the degree of riming remains challenging.

Even though the 2DVD provides state-of-the-art hydrometer particle observation, the 2DVD is challenging to maintain and not ideal for continuous unattended operation (Tokay et al. 2017). A viable alternative method utilizing collocated Micro Rain Radar (MRR, Löffler-Mang et al. 1999) and Particle Size and Velocity (Parsivel, Löffler-Mang and Joss 2000) distrometer is proposed in this study to derive the bulk snow density. Parsivel and MRR are reliable, robust, easy to maintain, and relatively affordable. Hence, they are widely used in the research community and typically collocated. The MRR is a vertically pointing frequency modulated continuous wave (FMCW) radar at 24.23 GHz. The radar transmitted radiation vertically upward, and



65 the hydrometeor above scattered a portion of the energy back to the antenna. The magnitude and frequency of the backscatter signal provide the vertical profiles of  $Z_{HH}$  and the  $Z_{HH}$  weighted fall velocity ( $V_z$ ) (Kneifel et al. 2011). Parsivel is a laser-based optical distrometer for simultaneous particle size and velocity measurements. As the hydrometeor passes through the laser beam generated by the transmitter, particle extinction leads to a decrease in the energy detected by the receiver. The amplitude of the energy reduction determines particle size, and the particle velocity is derived from the reduction duration.

70 Similar to Huang et al. (2010), the measured  $Z_{HH}$  from MRR is applied to constrain the probability of volume ratio of ice and liquid water ( $v_i$  and  $v_w$ ) on the simulated  $Z_{HH}$  from particle size distribution (PSD) of Parsivel in the proposed method. The bulk density of snow ( $\rho_{bulk}$ ) is consequently derived from the  $v_i$  and  $v_w$ , corresponding to the most consistently measured and simulated  $Z_{HH}$ . Subsequently, the measurement of  $Z_{HH}$  weighted fall velocity ( $V_z$ ) from MRR, regarded as the self-evaluation of our result, is compared with the calculated  $V_z$  from the derived bulk density and PSD measurement from Parsivel.

75 The consistency between the measured and calculated  $V_z$  ensures the reliability of the estimated bulk snow density. Finally, independent measurements of the liquid-equivalent snowfall rate observed by Pluvio evaluate the bulk snow density from the proposed method.

The main objective of this study is to evaluate the algorithm as introduced earlier. The data of the microphysical instruments, namely MRR, Parsivel, and Pluvio, from the International Collaborative Experiments for Pyeongchang 2018 Olympic and Paralympic Winter Games (ICE-POP 2018) Projects and its pre-campaign is applied to estimate the bulk density of snow. The performance and applicability of the proposed algorithm are examined using the ICE-POP data. The instruments and data are introduced in section 2. The methodology is detailed in section 3. The results are summarized in section 4. Finally, the conclusion is shown in section 5.

80

## 2 Instruments and Data Processing

85 The data of MRR, Parsivel, and Pluvio were collected during the ICE-POP 2018 (2017/2018 winter) and the pre-ICE-POP campaign (2016/2017 winter). The instruments were located in nineteen sites across the Gangwon region on the east coast of Korea (Kim et al. 2021). Five sites with collocated MRR and Parsivel were available for this study. These sites aligned across the Taebaek Mountains from mountain to coast are YPO (YongPyong Observatory), MHS (MayHills Supersite), CPO (Cloud Physics Observatory), BKC (BoKwang 1-ri Community Center), and GWU (Gangneung-Wonju National University),

90 respectively. The YPO, MHS, and CPO sites are in the mountainous region, while GWU and BKC sites are in the coastal area. The data available from these five sites during the pre-campaign and ICE-POP campaign are listed in Table 1.

The snow observation from Parsivel suffers from various issues due to the measuring principle (Battaglia et al. 2010). The minute PSD data was quality-controlled using the fall velocity filtering technique (Lee et al. 2015). The mean fall velocity and standard deviation ( $\sigma$ ) for a given diameter were calculated, and the particles that deviate from the mean fall velocity of more than one standard deviation were filtered. The quality-controlled data of Parsivel was subsequently processed for the  $Z_{HH}$

95



calculation. The third gate of  $Z_{HH}$  data from MRR was selected for retrieving snow density since some clutter contamination can be found in the first two gates.

The MRR and Parsivel have different measuring principles and designs. The measurement inconsistency between collocated MRR and Parsivel degrades the accuracy of estimating the bulk density. To ensure the observation consistency between MRR and Parsivel data and to minimize the measurement bias, the pure rain precipitation events (13-14 April 2018 and 22-23 April 2018) were selected to calculate the bias in rainfall rate between MRR and Parsivel. The data was quality controlled by examining the rainfall rate of the MRR, Parsivel, and collocated Pluvio. The rainfall rate measurements from Parsivel and Pluvio (a weighing gauge) were consistent with each other. Thus, the Parsivel PSD data was applied to the T-Matrix simulation to obtain  $Z_{HH}$ . The mean bias was derived after excluding one standard deviation outlier data. The mean bias values of each MRR are listed in Table 2. The results indicate that the MRR consistently underestimated the reflectivity from 2.1 to 10.2 dBZ. The MRR data have been bias-corrected by applying the bias values listed in Table 2.

### 3 Methodology

Hydrometeor is composed of solid ice and liquid water with a density of 0.92 ( $\rho_{ice}$ ) and 1.0 ( $\rho_{water}$ )  $g\ cm^{-3}$ , respectively. Therefore, the hydrometeor bulk density ( $\rho_{bulk}$ ) can be determined by its volume ratio of solid ice ( $v_i$ ) and liquid water ( $v_w$ ) as follows,

$$\rho_{bulk} = v_i \times 0.92 + v_w; \text{ g cm}^{-3}. \quad (1)$$

The sum of the values of  $v_i$  and  $v_w$  equals one or less than one if it contains air in the particle. Thus, the reflectivity factor ( $Z_{HH}$ ) can be calculated as follows under Rayleigh scattering assumption (Huang et al. 2010),

$$Z_{HH} = \left( \frac{\rho_{bulk}}{\rho_{ice}} \right)^2 \frac{|K_{ice}|^2}{|K_w|^2} \int D^6 N(D) dD; \text{ mm}^6 \text{ m}^{-3}. \quad (2)$$

The  $K_{ice}$  and  $K_w$  are the dielectric factors of solid ice and liquid water, respectively.  $D$  is the particle size, and  $N(D)$  is the particle size distribution. As shown in (1) and (2), the  $Z_{HH}$  is positively correlated to  $\rho_{bulk}$ . The higher hydrometer bulk density has a higher value of  $Z_{HH}$  for a given PSD. Hence, the  $Z_{HH}$ , the factor relating to the  $v_i$  and  $v_w$  of hydrometeor, can estimate the bulk density. Huang et al. (2010) utilized the C-band radar measurements on top of a 2DVD. The  $\rho_{bulk}$  was derived from (2) by applying the reflectivity from C-band radar and the PSD from 2DVD. However, the sampling size discrepancy of C-band radar resolution volume on top of 2DVD was neglected by Huang et al. (2010).

The bulk density estimation algorithm developed in this study is modified by Huang et al. (2010). Instead of scanning C-band radar and 2DVD, the collocated MRR (Micro Rain Radar, Löffler-Mang et al. 1999) and Parsivel are proposed to minimize the sampling size inconsistency. The estimated density is considered as "bulk" or "equivalent" density since the MRR  $Z_{HH}$  measurement is the summation of all hydrometeor within the sampling volume. The procedures of the proposed method are introduced in the following section, and the validation and discussion are described in the next section.





The  $Z_{HH}$  values were simulated from each Parsivel PSD measurement. Each  $Z_{HH}$  value was calculated using a rigorous T-matrix method with specified  $v_i$  and  $v_w$  (Vivekanandan et al. 1991; Bringi and Chandrasekar 2001). The T-matrix method is a fast numerical solution of Maxwell's equations to compute the scattering properties of particles. The shape of the hydrometeor is regarded as a symmetric sphere since the  $Z_{HH}$  measurement of the hydrometer was observed from the bottom of the snow  
130 particle by vertical pointing MRR. The mean and standard deviation of the canting angle are assumed  $0^\circ$  and  $20^\circ$ , respectively.

An example of simulated  $Z_{HH}$  from Parsivel observed snow PSD via T-matrix simulation with different combination of  $v_i/v_w$  and temperature is shown in Fig. 1. The results indicate that the simulated  $Z_{HH}$  values remain nearly identical when varying the temperature from  $-10$  to  $0^\circ\text{C}$ . On the other hand, the simulated  $Z_{HH}$  varies significantly when altering the composition of  $v_i/v_w$ . The lowest (highest) value of  $Z_{HH}$  was from the combination of  $v_i/v_w$  of  $1.0/0.0$  ( $0.0/1.0$ ), which was  
135 pure ice (rain) with a density of  $0.92$  ( $1.0$ )  $\text{g cm}^{-3}$ . The particle temperature was consequently assumed to have a constant value of  $0^\circ\text{C}$  in the following  $Z_{HH}$  T-matrix simulation. On the other hand, all possible combinations of  $v_i$  and  $v_w$  ranging from  $0.0$  to  $1.0$  were included in the T-matrix simulation of  $Z_{HH}$ .

A selected example of the simulated  $Z_{HH}$  from observed PSD with various combinations of  $v_i/v_w$  is shown in Figure 2. The observed PSD from Parsivel (Fig. 2a) was applied to the T-Matrix backscattering simulation. All possible combinations of  
140  $v_i/v_w$  were used to calculate simulated  $Z_{HH}$  (Fig. 2b). The corresponding bulk density was derived via (1) and shown as contour lines in Fig. 2b. The values of simulated  $Z_{HH}$  vary from  $-5$  to  $35$  dBZ (shaded color in Fig. 2b). The simulated  $Z_{HH}$  values increase as the increasing of the bulk snow density. In this selected case, the observed  $Z_{HH}$  from MRR was  $18.49$  dBZ (blue dash line in Fig. 2b). The observed  $Z_{HH}$  from MRR was thus applied to constrain the possible combination of  $v_i/v_w$  and bulk density. The possible ranges of  $v_i/v_w$  are  $0.0/0.02$  to  $0.3/0.0$ , shown as a dashed blue line in Fig. 2b. The corresponding bulk  
145 density are  $0.02$  and  $0.28$   $\text{g cm}^{-3}$ , respectively. The higher the fraction of ice (e.g.,  $v_i$ ), the higher bulk snow density values can be found in Fig. 2b. To determine the bulk snow density from possible combinations of  $v_i/v_w$ , bulk density with the maximum  $v_i$  is selected as suggested in Huang et al. (2010). The contour's maximum density,  $0.28$   $\text{g cm}^{-3}$ , is determined as the estimated bulk density by assuming  $v_w$  is  $0$ .

Moreover, liquid water's dielectric constant value is higher than that of solid ice. Consequently, the magnitude and variation  
150 of retrieved density are influenced mainly by  $v_w$ , as shown in Fig. 2b. The change of  $v_w$  can be adequately obtained in the proposed method. Consequently,  $v_w$  can be regarded as "bulk water fraction" which can also be estimated in the proposed method besides the bulk density and will be analyzed in the following section.

This study will use two approaches to evaluate the density derived from the proposed method with collocated MRR and Parsivel measurements. First, the bulk density was self-verified with the reflectivity-weighted fall velocity ( $V_Z$ ). The fall  
155 velocity measurements from MRR ( $V_Z^{MRR}$ ) and the "density-calculated" fall velocity derived from bulk density ( $V_Z^{\rho_{bulk}}$ ) are compared to ensure the consistency of observed and calculated  $V_Z$ .

The terminal fall velocity of particle size  $D$ ,  $V(D)$ , was computed from derived bulk density ( $\rho_{bulk}$ ) as follows (Rogers and Yau 1989),



$$V(D) = \left( \frac{4}{3} \frac{g}{C_d} \frac{\rho_{bulk}}{\rho_{air}} \right)^{0.5} D^{0.5} \quad (3)$$

160 The  $C_d$  is the drag coefficient and equals to 0.5 for the sphere hydrometeor assumption.  $g$  is the gravity constant ( $9.81 \text{ kg m}^{-2}$ ).  $\rho_{air}$  is the air density which is assumed as constant ( $1.29 \times 10^{-3} \text{ g cm}^{-3}$ ) in the calculation. Subsequently, the corresponding  $V_z^{\rho_{bulk}}$  can be obtained from  $V(D)$  as following,

$$V_z^{\rho_{bulk}} = \frac{\sum Z(\rho_{bulk}, D) V(D) N(D) dD}{\sum Z(\rho_{bulk}, D) N(D) dD} \quad (4)$$

The  $Z(\rho_{bulk}, D)$  indicates the reflectivity factor from retrieved bulk density ( $\rho_{bulk}$ ).  $N(D)$  represents the number concentration of the particle size  $D$  obtained from Parsivel.

165 The comparison of the  $V_z^{\rho_{bulk}}$  and the  $V_z^{MRR}$  is considered as a quality control procedure of the retrieved bulk density. This procedure utilizes independent measurement,  $V_z^{MRR}$ , which is not used in the bulk density retrieval process. As discussed in the previous section, the proposed retrieval technique requires well-calibrated data from MRR and Parsivel. Nevertheless, the snow observations from Parsivel and MRR suffered various issues due to measuring principles. The  $V_z$  criteria of the five sites are determined as the absolute value of the  $V_z$  mean bias of the sites plus one standard deviation of the bias. The  $V_z$  criteria are applied to each site to remove inadequate bulk density estimation. The corresponding  $V_z$  criteria values are shown in Table 3.

170 The second approach to evaluating the retrieved bulk density is examining the liquid-equivalent snowfall rate (SR,  $\text{mm hr}^{-1}$ ). The collocated Pluvio was utilized to investigate the performance of the derived bulk density. The SR was calculated with the derived bulk density  $\rho_{bulk}$ , fall velocity  $V(D)$  and the PSD from Parsivel measurement as shown in (5).

$$SR = 3.6 \sum_{i=1}^{32} \frac{\pi \rho_{bulk}}{6} D^3 \times V(D_i) N(D_i) \quad (5)$$

The measured and calculated SR are integrated into 5 min resolution (Li et al. 2018) to avoid instant fluctuation in the comparison. The SR calculated from the derived density is examined with the Pluvio SR, independent of the Parsivel and MRR observations. In addition, the  $\rho_{bulk} - D_0$  relation is also derived for analysis. Once the PSD is obtained from Parsivel, the median-volume diameter ( $D_0$ ) defined in (6) can be derived (Brandes et al. 2007),

$$\int_{D_{min}}^{D_0} D^3 N(D) dD = \int_{D_0}^{D_{max}} D^3 N(D) dD \quad (6)$$

where one-half of the precipitation volume is contained in particles smaller than  $D_0$  and one-half is contained in particles larger than  $D_0$ .

## 4 Results

185 The bulk density estimation has been applied to all available data during the ICE-POP 2018 and its pre-campaign, as listed in Table 1. There are 17 events: five sites with collocated MRR and Parsivel and four with Pluvio. The density-calculated fall



velocity ( $V_Z^{\rho_{bulk}}$ ) will first be examined with MRR measured fall velocity ( $V_Z^{MRR}$ ). The purpose is to remove inadequate bulk density retrieval due to MRR and Parsivel measurement issues. Subsequently, the liquid-equivalent snowfall rate (SR) will be validated by collocated Pluvio measurements. The statistical performance of retrieved bulk density will be investigated by comparing the SR. Furthermore, the detailed analysis of the two selected events will be illustrated by examining their environmental condition, precipitation type, and the spatiotemporal evolution of retrieved bulk density and bulk water fraction.

#### 4.1 Reflectivity-weighted ( $V_Z$ )

The normalized number density function of measured  $V_Z^{MRR}$  from MRR and "density-calculated"  $V_Z^{\rho_{bulk}}$  from PSD of five sites are shown in Fig. 3. The  $V_Z^{MRR}$  and  $V_Z^{\rho_{bulk}}$  are in agreement with each other. Most of the fall velocities were less than 2 m s<sup>-1</sup>. In addition, MHS, CPO, and GWU sites had second peak values of about 2.0-3.0 m s<sup>-1</sup> and showed reasonably consistent values. The BKC sites had the most consistency of velocity. On the other hand, the GWU site had the most discrepancy, which  $V_Z^{\rho_{bulk}}$  was sometimes higher than  $V_Z^{MRR}$ . The bias and standard deviation values (Table 3) are about -0.27 m s<sup>-1</sup> to 0.03 m s<sup>-1</sup> and 0.67 to 0.94 m s<sup>-1</sup>, respectively. In general, the  $V_Z^{\rho_{bulk}}$  values of YPO, MHS, and CPO (BKC and GWU) are slightly lower (higher) than  $V_Z^{MRR}$ . The bias and standard deviation values are -0.07 m s<sup>-1</sup> and 0.80 m s<sup>-1</sup>, respectively. A more detailed comparison will be shown in the selected case study.

The deviation of the calculated  $V_Z$  is partly attributed to the idealized equation of terminal fall velocity in (3) and (4). In the  $V_Z$  calculation, particles are assumed to be spheres, and the drag coefficient is 0.5. The various shapes and falling behaviors of ice-phase and mixing-phase particles induce noise and deviation when comparing MRR  $V_Z$  measurements. Moreover, various measurement issues of MRR and Parsivel also influence some inconsistency. Subsequently, the  $V_Z$  criteria value determined from each site's standard deviation was obtained to remove inadequate bulk density retrieval. The  $V_Z$  criteria values are about 0.84 to 1.8 m s<sup>-1</sup> (Table 3). The retrieval of the difference between  $V_Z^{\rho_{bulk}}$  and  $V_Z^{MRR}$  greater than  $V_Z$  criteria was removed in the following analysis.

#### 4.2 Liquid-equivalent snowfall rate (SR)

After removing the inadequate bulk density retrievals with the  $V_Z$  criteria, the density-derived SR is obtained and compared with collocated Pluvio measurements. Fig. 4 demonstrates the normalized number density function of the density-derived and measured SR of four sites. The majority of the SR values are less than 2.0 mm hr<sup>-1</sup>. Most retrieved and observed SR are around the 1-to-1 line, indicating that the retrieved bulk density SR agrees with the Pluvio SR measurement. Some fractional data scatter away from the 1-to-1. The correlation coefficient values are between 0.52 and 0.74, as shown in Table 3. The bias and standard deviation values of each site are about -0.27 to -0.11 mm hr<sup>-1</sup> and 0.73 to 1.09 mm hr<sup>-1</sup>, respectively. The overall mean bias and mean standard deviation values of five sites are -0.18 mm hr<sup>-1</sup> and 0.93 mm hr<sup>-1</sup>, respectively. The results indicate that the density-derived SR is slightly lower than the Pluvio-observed SR. It is postulated that the attenuation effect caused by the accumulated snow atop the MRR antenna induced the underestimation of the reflectivity and thus the retrieved bulk density



and SR. Even though the MRRs deployed in ICE-POP were equipped with heating capability, notes taken during the observation indicates the presence of a significant amount of accumulated snow on the antenna. Thus, some inconsistency  
220 between MRR reflectivity and Parsivel PSD can be noticed. More discussion will be shown in the next section.

Two snow events, 28 February 2018 and 7 March 2018, from the ICE-POP 2018, are selected for further investigation. The synoptic pattern of these two events was characterized as warm-low, according to Kim et al. (2021), with the low pressure situated to the south of the polar jet. Most of the precipitation was in the southern and eastern parts of Korea. The warm and moist air was transported from the Yellow Sea and East Sea. This moisture air forms supercooled water as it encounters the  
225 steep Taebaek mountain, which benefits the growth of ice-phased particles by riming (Kim et al. 2021). The event on 28 February 2018 had the most intense precipitation rate, and accumulated snowfall during the ICE-POP (Gehring et al. 2020) is investigated comprehensively. The data of the MHS site is examined to understand the pros and cons of the proposed bulk density estimation algorithm. The derived bulk density and the weather factors of the five sites aligned from the Taebaek mountain to the coast (from southwest to northeast are YPO, MHS, CPO, BKC, and GWU) from the event of 7 March 2018  
230 are investigated to understand the performance of derived bulk density in different environment condition.

#### 4.3 Case study: 28 February 2018

The time series of observational data from the MHS site on 28 February 2018 is shown in Fig 5, the mid-level precipitation was evaporated and observed by MRR from 00 to 03 UTC (Fig. 5c). Precipitation reached the surface at 03 UTC and continued until 16 UTC (Fig. 5b), the precipitation gradually weakening after 16 UTC (Gehring et al. 2020). Both retrieved bulk density  
235 and bulk water fraction decreased gradually from 0.4 to 0.05 g cm<sup>-3</sup> and 0.5 to 0.0 between 03 and 05 UTC (Fig. 5a), while the temperature slowly dropped from 5°C to 0°C. The derived bulk density between 04 and 16 UTC was low (less than 0.2 g cm<sup>-3</sup>), and the bulk water fraction was nearly zero. The MASC data show aggregate particles during this period (Gehring et al., 2020). The precipitation gradually weakened after 16 UTC, and the bulk density increased again (0.4 to 1 g cm<sup>-3</sup>). The graupel and small particles were identified as the temperature continued to drop till the end of the day, according to MASC data  
240 (Gehring et al., 2020). The higher retrieved bulk density during the weakening period is consistent with the hydrometeor classification of MASC observation in Gehring et al. (2020).

The velocities from MRR ( $V_Z^{MRR}$ ) and calculated from retrieved bulk density ( $V_Z^{P_{bulk}}$ ) are shown in Fig. 5e. The increasing values of  $V_Z^{MRR}$  from 15 UTC to 18 UTC is consistent with the  $V_Z^{P_{bulk}}$  calculated from bulk density. However, a pronounced discrepancy between the  $V_Z^{P_{bulk}}$  and the  $V_Z^{MRR}$  can be noticed at 06 UTC and between 09 and 14 UTC (Fig. 5e). The fall  
245 velocity inconsistency suggests that the retrieved bulk density is not derived adequately. It can be noticed that there was a pronounced  $Z_{HH}$  drop in MRR measurement around 06 UTC and 09 to 13 UTC (Fig. 5d), which is inconsistent with PSD measurement (Fig. 5c). This implies that significant snow accumulation on the antenna, particularly associated with large-sized aggregated snow at 06 UTC (Fig. 5c), likely results in strong attenuation. This leads to the degraded performance of the



bulk density retrieval algorithm. The unreasonable retrieval data is identified by  $V_z$  criteria introduced in the previous section  
250 and is regarded as less credible (gray area in Fig. 5).

In Fig. 5f, the consistency of the bulk density calculated SR and observed SR from Pluvio can be found from 03 to 08 UTC  
and 15 UTC to 24 UTC. The underestimation of the bulk density calculated SR from 08 to 15 UTC was caused by the attenuated  
MRR measurement. The  $V_z$  criteria also identify the underestimated SR. Overall, both the  $V_z^{\rho_{bulk}}$  and SR show good  
agreement with the MRR and Pluvio, except the period with inadequate bulk density. The result indicates that the algorithm  
255 can derive bulk density adequately.

The fall velocity-diameter relation examines the overall microphysical characteristics of the event in Fig. 6. Distinct  
characteristics of the fall velocity-diameter relation can be noticed before 04 and after 16 UTC. In Figs. 6a and c, most of the  
hydrometeor size was less than 2 mm (Fig. 5b), and fall velocity was more significant than  $1 \text{ m s}^{-1}$  (Fig. 5e, close to the fall  
velocity-diameter relation of rain and graupel) before 04 UTC and after 16 UTC. Before 04 UTC, the fog near the surface and  
260 nimbostratus was observed by W-band radar (Gehring et al. 2020). In addition, the temperature was above  $0^\circ\text{C}$ , and the particle  
size was less than 5 mm. These features suggest possible wet snow, small raindrops, and drizzle. After 16 UTC, the graupel  
and small particles with near zero environment temperature were identified by MASC (Gehring et al. 2020). From 04 to 16  
UTC (Fig. 6 b), the particles were aggregate-like with a lower derivation density. The particle size was 8 to 20 mm (Fig. 5b  
and Fig. 6b). More particles were found between the lines of graupel and dry dendrites fall velocity-diameter relations.

#### 265 4.4 Case study: 7 March 2018

Both the 7 March and 28 February events share similar larger-scale conditions. The difference between these two events is  
that the precipitation on the 7 March was relatively weaker yet persisted for longer than the 28 February event. An east-moving  
trough from east China became a potential vorticity streamer, which produced prominent precipitation (Gehring et al. 2020).  
The low-pressure system developed over the Korean peninsula and produced intensive precipitation. Besides the similarity in  
270 larger-scale conditions, the microphysical characteristics of precipitation systems share similar behaviors in these two cases.  
The bulk density rapidly increased in most sites (Fig. 7 to 11) as the nimbostratus weakened and dissipated into the shallow  
convection (about 03 UTC on 08 March 2018). The bulk density also increased as the temperature decreased in YPO, MHS,  
and CPO sites (Fig. 7a,c to 9a,c). The five sites share similar tendencies of derived bulk density, bulk water fraction, PSD,  $Z_{HH}$   
profile, and SR. The intensive precipitation system associated with the low-pressure system started at 10 UTC on 7 March and  
275 gradually dissipated near 04 UTC on 8 March. The weakened precipitation with shallow convections can be found from 08  
UTC to 19 UTC on 8 March.

The overall bulk density and bulk water fraction in the GWU site (Fig. 11) are the highest in all sites. In contrast, the YPO  
(Fig. 7) site demonstrates a relatively lower magnitude of bulk density and bulk water fraction, especially after 04 UTC on 8  
March. The contrast may be attributed to their geographical environment, as the YPO site is located in the westernmost  
280 mountainous area of the five sites. In contrast, the GWU site is located on the east coast, which faces abundant moisture from



the East Sea. Gradual increase of density as well as the liquid water content can also be found in the distribution of fall velocity versus the diameter from MHS, BKC, to the GWU sites (Fig. 12). The distributions of the GWU site mostly feature particles concentrated around the fall velocity-diameter relation of rain. While in MHS and BKC sites, especially the MHS site, data are distributed more discretely and scattered between the relation of rain to the relation of dry dendrites. Overall, the features of sites due to the geographical and synoptic environments are successfully revealed by the retrieved bulk density and bulk water fraction, which are in accord with the distributions of all velocity-diameter relations.

The YPO, MHS, and CPO sites had continual low bulk density and bulk water fraction values (about 0.1 to 0.2 g cm<sup>-3</sup>, Figs. 7a-9a) at the beginning of the precipitation. They gradually dissipated at 04 UTC on 8 March. The MRR reflectivity profiles indicate an intensive precipitation system up to 5 km (Figs. 7c-9c) from 10 UTC on 7 March to 04 UTC on 8 March. The PSD was featured with large particle size (Figs. 7b-9b) and aggregates-like particles (Gehring et al. 2020). The coastal sites began with nimbostratus cloud and high bulk density values (Figs. 10a,b-11a,b), 10 to 13 UTC for BKC and 10 to 19 UTC for GWU on 7 March, followed by similar low bulk density as other sites till 04 UTC on 8 March. The high-density period in the beginning corresponds to a higher bulk water fraction derived. Hence, it implies more liquid-water constituents, which can confirm the distribution of fall velocity and diameter. More data concentrate near the rain relation from 08 to 19 UTC 7 March (Fig. 12c) than 19 UTC to 03 UTC on 8 March in GWU site (Fig. 12f). The higher density initially in MHS and BKC sites are also confirmed by the alike contrast between 08 to 19 UTC on 7 March (Figs. 12a, b) than 19 UTC to 03 UTC on 8 March (Figs. 12d, e).

After 04 UTC on 8 March, all sites featured high bulk density and bulk water fraction (Figs. 9a-11a). The PSDs were mainly small particles (Figs. 9b-11b). According to MRR measurements, the precipitation systems were weaker and shallower (Figs. 9c-11c) compared to the period with low bulk density. The  $V_z$  of particles also transitioned from consistently low values to slightly higher and more noisy values (Figs. 9e-11e), suggesting high-density particles with high fall velocity. Compared to 19 UTC on 7 March to 03 UTC on 8 March (Figs. 12d, e, and f), the velocity-diameter velocity relation from 04 to 12 UTC on 8 March has a more consistent relation of rain (Figs. 12g, h, and i). After 12 UTC, more particles were distributed between the relation of rain and graupel (Fig. 12j, k, and l). Before the dissipation of precipitation (around 12 UTC on 8 March), a sudden decrease of  $V_z$  and an increase in particle size were found in YPO, MHS, and CPO sites. Low bulk density in YPO, MHS, CPO, and BKC sites also captured this feature.

Moreover, the good agreements between the Pluvio SR and the derived SR calculated from all sites' bulk density can be noticed in Figs. 7f, 8f, 10f, 11f. The Pluvio is not available at the CPO site. Two distinct types of precipitation structures (according to MRR) and microphysical characteristics (bulk density, bulk water fraction, PSD) can be noticed in Figs. 7-11. One has deeper and more intensive precipitation structures, higher bulk density, and bulk water fraction, and is contained with smaller particles. Overall, the estimation of the bulk density and the bulk water fraction demonstrates the contrast between sites of different geographical locations and captures the evolution of the precipitation system.





#### 4.5 Statistical analysis of bulk density and bulk water fraction

The retrieved bulk density and bulk water fraction are investigated statistically to understand the microphysical characteristics of the winter precipitation systems from ICE-POP 2018 and its pre-campaign. The number density function of retrieved bulk density and observed median-volume diameter ( $D_0$ ) of all sites are shown in Fig. 13. The bulk density decreases exponentially as  $D_0$  increases. The majority of the particle is consistent with  $\rho_{bulk} - D_0$  relation of Brandes et al. (2007), which utilized the data of 52 storm days from the Front Range in eastern Colorado during October–April 2003 to 2005 of a ground-based two-dimensional video disdrometer. The data of Brandes et al. (2007) is dominated by almost spherical aggregates having near-exponential or superexponential size distributions.

On the other hand, the  $\rho_{bulk} - D_0$  relation from Heymsfield et al. (2004) shows slightly lower bulk density than this study. Heymsfield et al. (2004) utilized the aircraft data collected from two field programs, namely the Atmospheric Radiation Measurement (ARM) program, Cirrus Regional Study of Tropical Anvils and Cirrus Layers (CRYSTAL) Florida Area Cirrus Experiment (FACE) in southern Florida during July 2002. The ARM data is mostly ice clouds formed primarily through large-scale ascent, and the CRYSTAL observations are mainly from convectively generated cirrus anvils. The consistent  $\rho_{bulk} - D_0$  relations between ICE-POP 2017/2018 and Brandes et al. (2007) can be attributed to the similar environmental conditions of the two studies. This results indicate that the proposed bulk density estimation algorithm can derive accurate retrievals with consistent microphysical characteristics in similar environmental conditions.

To further understand the microphysical characteristics of winter precipitation, each site's retrieved bulk density and bulk water fractions are divided into warm-low (nine cases) and cold-low (five cases) events according to the synoptic condition (Kim et al. 2021; Gehring et al. 2020). As shown in Fig. 14a, the mean values of bulk density of warm-low events from the mountain site (YPO) to the coastal site (GWU) are about 0.09 to 0.25 g cm<sup>-3</sup>. The GWU site has the highest bulk density. On the other hand, the mean values of bulk density of cold-low events from YPO to GWU are about 0.07 to 0.12 g cm<sup>-3</sup> (Fig. 14b). The overall bulk density values are lower in cold-low events than in warm-low events.

In Fig. 14c and d, more than 90% of bulk water fractions are less than 0.03 for warm- and cold-low events. The YPO site has the lowest bulk water fraction, especially the cold-low events that remain lower than 0.1. The mean value of the top 5% of the bulk water fraction of each site is obtained for further investigation. The warm-low event has a relatively higher bulk water fraction than cold-low events due to warmer and moister environments. The values of bulk water fraction gradually increase from the mountain site (YPO) to the coastal site (GWU) for both warm- and cold-low events. The mean values of the top 5% bulk water fraction of MHS to GWU site for warm-low events are 0.02 to 0.50, and the cold-low events are 0.12 to 0.30. The increasing feature of bulk water fraction from YPO to GWU is the same as that of bulk density. These results indicate that the winter precipitation systems of coastal sites with warmer and moister environments have higher bulk water fraction than mountain sites.



## 5 Conclusion

345 The density of snow, one of the key characteristics, varies with the microphysics processes and imposes weather conditions. The variations inherently involve complex behaviors and require more investigations. In the study, the snow density is derived by compositing collocated MRR and Parsivel data, which can be acquired easily. In the proposed method, the PSD from the Parsivel is applied to T-matrix backscattering simulation and compared with the  $Z_{HH}$  from MRR. The bulk density and bulk water fraction are derived from comparing simulated and calculated  $Z_{HH}$ . The high sensitivity of  $Z_{HH}$  to the liquid portion of  
350 the particle led to precise bulk water fraction estimation. It implied better capability of the density variation due to bulk water fraction change (ex. melting) in the proposed method in this study.

The reflectivity-weighted fall velocity ( $V_z$ ) of MRR is considered as the self-evaluation of the retrieved bulk density and water fraction. Consistency of measured  $V_z$  from MRR and calculated  $V_z$  from retrieved bulk density from 09 to 15 UTC on 28 February 2018 is noticed. It is postulated that the attenuation effect mainly causes the  $V_z$  discrepancy due to the accumulated  
355 snow on the MRR antenna. The  $V_z$  criteria is proposed to mitigate uncertainties in bulk density retrieval. The performance of the retrieved bulk density is validated by comparing independent measurements of snowfall rate (SR) from collocated Pluvio and calculated SR from bulk density. The consistency of SR has been greatly improved after applying the  $V_z$  criteria. The correlation coefficient values can be up to 0.74, and the mean bias is about  $-0.18 \text{ mm hr}^{-1}$ . General consistency between the measured and the bulk density-calculated SR was found in all available cases of the four sites during the ICE-POP 2018  
360 campaign.

The bulk density and bulk water fraction of two events with warm low synoptic patterns (28 February 2018 and 7<sup>th</sup> to 8<sup>th</sup> March 2018) were investigated. In these two cases, similar demarcations that separate lower and higher-density periods were found in similar synoptic conditions. During the transition, particles' bulk density and fall velocity rose with decreasing particle size while the convection precipitation dissipated. The microphysical similarity of these two events confirms the dependence  
365 of the micro-scale factors on the synoptic conditions.

The contrastive bulk density and bulk water fraction between mountain sites (YPO and MHS, lower bulk density and bulk water fraction) and coastal sites (BKC and GWU, higher bulk density and bulk water fraction) indicates the geographical and synoptic environmental effects on distinct microphysical characteristics of winter precipitation systems of each site. Overall, the derivations demonstrated good accordance with the fall speed, the diameter of the particle, and the  $V_z$  and SR in time series,  
370 providing an insightful perspective in microphysics analysis.



### Competing interests

The contact author has declared that none of the authors has any competing interests.

### Acknowledgments

380 The authors greatly appreciate the participants in the World Weather Research Programme research development project  
and forecast demonstration project “International Collaborative Experiments for Pyeongchang 2018 Olympic and Paralympic  
winter games” (ICE-POP 2018) hosted by the Korea Meteorological Administration (KMA). We would like to thank Sang-  
Won Joo, Yong-Hee Lee, Kwang-Deuk Ahn, Namwon Kim, and Seung-bo Choi at the KMA for their support for the ICE-  
POP 2018 field campaign. The authors are grateful to Walter Petersen, Ali Tokay, Patrick Gatlin, and Matthew Wingo at  
385 NASA for providing the MRR and PARSIVEL instruments and processing the PARSIVEL data. We would also like to thank  
Byung-Gon Kim at Gangneung-Wonju National University and Byung-Chul Choi at the High Impact Weather Research  
Center of the KMA for sharing their instruments. This work was funded by the National Science and Technology Council of  
Taiwan under Grant 112 WFA0710420 and by the Korea Meteorological Administration Research and Development Program  
under Grant RS-2023-00237740.

390

395

400

405



## References

- Battaglia, A., Rustemeier, E., Tokay, A., Blahak, U., and Simmer, C.: PARSIVEL Snow Observations: A Critical Assessment, *J. Atmos. Oceanic Technol.*, 27, 333-344, <https://doi.org/10.1175/2009JTECHA1332.1>, 2010.
- Brandes, E. A., Ikeda, K., Zhang, G., Schönhuber, M., and Rasmussen, R. M.: A Statistical and Physical Description of Hydrometeor Distributions in Colorado Snowstorms Using a Video Disdrometer, *J. Appl. Meteorol. Climatol.*, 46, 634-650, <https://doi.org/10.1175/JAM2489.1>, 2007.
- Bringi, V., and Chandrasekar, V.: *Polarimetric Doppler Weather Radar: Principles and Applications*, Cambridge: Cambridge University Press, doi:10.1017/CBO9780511541094, 2001.
- Chang, W. Y., Lee, G., Jou, B. J. D., Lee, W. C., Lin, P. L., and Yu, C. K.: Uncertainty in Measured Raindrop Size Distributions from Four Types of Collocated Instruments. *Remote Sens.* 12, 1167, <https://doi.org/10.3390/rs12071167>, 2020.
- Gehring, J., Ferrone, A., Billault-Roux, A. C., Besic, N., Ahn, K. D., Lee, G., and Berne, A.: Radar and ground-level measurements of precipitation collected by EPFL during the ICE-POP 2018 campaign in South-Korea, *Earth Syst. Sci. Data*, 13, 417-433, <https://doi.org/10.5194/essd-13-417-2021>, 2021.
- Heymsfield, A. J.: A Comparative Study of the Rates of Development of Potential Graupel and Hail Embryos in High Plains Storms, *J. Atmos. Sci.*, 39, 2867-2897. [https://doi.org/10.1175/1520-0469\(1982\)039<2867:ACSOTR>2.0.CO;2](https://doi.org/10.1175/1520-0469(1982)039<2867:ACSOTR>2.0.CO;2), 1982.
- Heymsfield, A. J., Bansemer, A., Schmitt, C., Twohy, C., and Poellot, M. R.: Effective Ice Particle Densities Derived from Aircraft Data, *J. Atmos. Sci.*, 61, 982-1003, [https://doi.org/10.1175/1520-0469\(2004\)061<0982:EIPDDF>2.0.CO;2](https://doi.org/10.1175/1520-0469(2004)061<0982:EIPDDF>2.0.CO;2), 2004.
- Huang, G., Bringi, V. N., Cifelli, R., Hudak, D., and Petersen, W. A.: A Methodology to Derive Radar Reflectivity-Liquid Equivalent Snow Rate Relations Using C-Band Radar and a 2D Video Disdrometer, *J. Atmos. Oceanic Technol.*, 27, 637-651, <https://doi.org/10.1175/2009JTECHA1284.1>, 2010.
- Huang, G. J., Bringi, V. N., Moisseev, D., Petersen, W. A., Bliven, L., and Hudak, D.: Use of 2D-video disdrometer to derive mean density-size and Ze-SR relations: Four snow cases from the light precipitation validation experiment, *Atmos. Res.*, 153, 34-48, <https://doi.org/10.1016/j.atmosres.2014.07.013>, 2015.
- Huang, G.-J., Bringi, V. N., Newman, A. J., Lee, G., Moisseev, D., and Notaroš, B. M.: Dual-wavelength radar technique development for snow rate estimation: a case study from GCPEX, *Atmos. Meas. Tech.*, 12, 1409-1427, <https://doi.org/10.5194/amt-12-1409-2019>, 2019.
- Kneifel, S., Maahn, M., Peters, G., and Simmer, C.: Observation of snowfall with a low-power FM-CW K-band radar (Micro Rain Radar), *Meteorol. Atmos. Phys.*, 113, 75-87, doi: 10.1007/s00703-011-0142-z, 2011.
- Kim, K., Bang, W., Chang, E. C., Tapiador, F. J., Tsai, C.-L., Jung, E., and Lee, G.: Impact of wind pattern and complex topography on snow microphysics during International Collaborative Experiment for PyeongChang 2018 Olympic and Paralympic winter games (ICE-POP 2018), *Atmos. Chem. Phys.*, 21, 11955-11978, <https://doi.org/10.5194/acp-21-11955-2021>, 2021.



- 440 Lee, J. E., Jung, S. H., Park, H. M., Kwon, S., Lin, P. L., and Lee, G. W.: Classification of Precipitation Types Using Fall Velocity–Diameter Relationships from 2D-Video Distrometer Measurements, *Adv. Atmos. Sci.*, 32, 1277–1290, <https://doi.org/10.1007/s00376-015-4234-4>, 2015.
- Li, H., Moisseev, D., and von Lerber, A.: How Does Riming Affect Dual-Polarization Radar Observations and Snowflake Shape? *J. Geophys. Res.*, 123, 6070–6081, <https://doi.org/10.1029/2017JD028186>, 2018.
- 445 Löffler-Mang, M., Kunz, M., and Schmid, W.: On the performance of a low-cost K-band Doppler radar for quantitative rain measurement, *J. Atmos. Oceanic Technol.*, 16, 379–387, [https://doi.org/10.1175/1520-0426\(1999\)016<0379:OTPOAL>2.0.CO;2](https://doi.org/10.1175/1520-0426(1999)016<0379:OTPOAL>2.0.CO;2), 1999.
- Löffler-Mang, M., and Joss, J.: An Optical Disdrometer for Measuring Size and Velocity of Hydrometeors, *J. Atmos. Oceanic Technol.*, 17, 130-139. [https://doi.org/10.1175/1520-0426\(2000\)017<0130:AODFMS>2.0.CO;2](https://doi.org/10.1175/1520-0426(2000)017<0130:AODFMS>2.0.CO;2), 2000.
- 450 Morrison, H., Milbrandt, J. A., Bryan, G. H., Ikeda, K., Tessendorf, S. A., and Thompson, G.: Parameterization of Cloud Microphysics Based on the Prediction of Bulk Ice Particle Properties. Part II: Case Study Comparisons with Observations and Other Schemes, *J. Atmos. Sci.*, 72, 312-339. <https://doi.org/10.1175/JAS-D-14-0066.1>, 2015.
- Mroz, K., Battaglia, A., Nguyen, C., Heymsfield, A., Protat, A., and Wolde, M.: Triple-frequency radar retrieval of microphysical properties of snow, *Atmos. Meas. Tech.*, 14, 7243–7254, <https://doi.org/10.5194/amt-14-7243-2021>, 2021.
- 455 Pruppacher, H. R., and Klett, J. D.: *Microphysics of Clouds and Precipitation*, *Aerosol Science and Technology*, 28:4, 381-382, <https://doi.org/10.1007/978-0-306-48100-0>, 1997.
- Roebber, P. J., Bruening, S. L., Schultz, D. M., and Cortinas, J. V., Jr.: Improving Snowfall Forecasting by Diagnosing Snow Density, *Wea. Forecasting*, 18, 264-287. [https://doi.org/10.1175/1520-0434\(2003\)018<0264:ISFBDS>2.0.CO;2](https://doi.org/10.1175/1520-0434(2003)018<0264:ISFBDS>2.0.CO;2), 2003.
- Rogers, R. R., and Yau, M. K.: *A short course in cloud physics*, Pergamon Press, Oxford, 1989.
- 460 Tokay, A., D’Adderio, L. P., Porcù, F., Wolff, D. B., and Petersen, W. A.: A Field Study of Footprint-Scale Variability of Raindrop Size Distribution, *J. Hydrometeor.*, 18, 3165-3179, <https://doi.org/10.1175/JHM-D-17-0003.1>, 2017.
- Yuter, S. E., Kingsmill, D. E., Nance, L. B., Löffler-Mang, M.: Observations of Precipitation Size and Fall Speed Characteristics within Coexisting Rain and Wet Snow, *J. Appl. Meteor. Climatol.*, 45, 1450–1464, <https://doi.org/10.1175/JAM2406.1>, 2006.
- 465 Vivekanandan, J., Adams, W. M., and Bringi, V. N.: Rigorous Approach to Polarimetric Radar Modeling of Hydrometeor Orientation Distributions, *J. Appl. Meteor. Climatol.*, 30, 1053-1063, [https://doi.org/10.1175/1520-0450\(1991\)030<1053:RATPRM>2.0.CO;2](https://doi.org/10.1175/1520-0450(1991)030<1053:RATPRM>2.0.CO;2), 1991.
- Zhang, G., Luchs, S., Ryzhkov, A., Xue, M., Ryzhkova, L., and Cao, Q.: Winter Precipitation Microphysics Characterized by Polarimetric Radar and Video Disdrometer Observations in Central Oklahoma, *J. Appl. Meteor. Climatol.*, 50, 1558-1570. <https://doi.org/10.1175/2011JAMC2343.1>, 2011.
- 470 Zhang, Y., Zheng, H., Zhang, L., Huang, Y., Liu, X., and Wu, Z.: Assessing the Effect of Riming on Snow Microphysics: The First Observational Study in East China, *J. Geophys. Res.*, 126, <https://doi.org/10.1029/2020JD033763>, 2021.



## Figures and Tables

475

**Table 1: Data availability of MRR (x), Parsivel (v), and Pluvio (o) for YPO, MHS, CPO, BKC, and GWU site during pre-campaign and ICE-POP campaign.**

Dates \ Site	YPO	MHS	BKC	GWU	CPO
2017/1/4~2017/1/5	v, x	v, x			v, x
2017/1/8	v, x	v, x			v, x
2017/1/29~2017/1/30	v, x	v, x			v, x
2017/2/21~2017/2/22	v, x	v, x			v, x
2017/3/1~2017/3/2	v, x	v, x			v, x
2017/3/14	v, x	v, x			v, x
2017/12/9~2017/12/10	v, x, o	v, x, o	v, x, o	v, x, o	v, x
2017/12/24	v, x, o	v, x, o	v, x, o	v, x, o	v, x
2018/1/7~2018/1/8	v, x, o	v, x, o	v, x, o	v, x, o	v, x
2018/1/16	v, x, o	v, x, o	v, x, o	v, x, o	v, x
2018/1/22	v, x, o	v, x, o	v, x, o	v, x, o	v, x
2018/1/30	v, x, o	x, o	v, x, o	v, x, o	v, x
2018/2/28~2018/3/1	v, x, o	v, x, o	v, x	v, x, o	v, x
2018/3/4~2018/3/5	v, x, o	v, x, o	v, x, o	v, x, o	v, x
2018/3/7~2018/3/8	v, x, o	v, x, o	v, x, o	v, x, o	v, x
2018/3/14~2018/3/15	v, x, o	v, x, o	v, x, o	v, x, o	v, x
2018/3/20~2018/3/21	v, x, o	v, x, o	v, x, o	v, x, o	v, x

480

**Table 2: MRR bias of YPO, MHS, CPO, BKC, and GWU sites derived from rain events.**

site \ MRR bias	YPO	MHS	CPO	BKC	GWU
mean	-8.7 dBZ	-10.2 dBZ	-7.4 dBZ	-2.1 dBZ	-5.8 dBZ

485

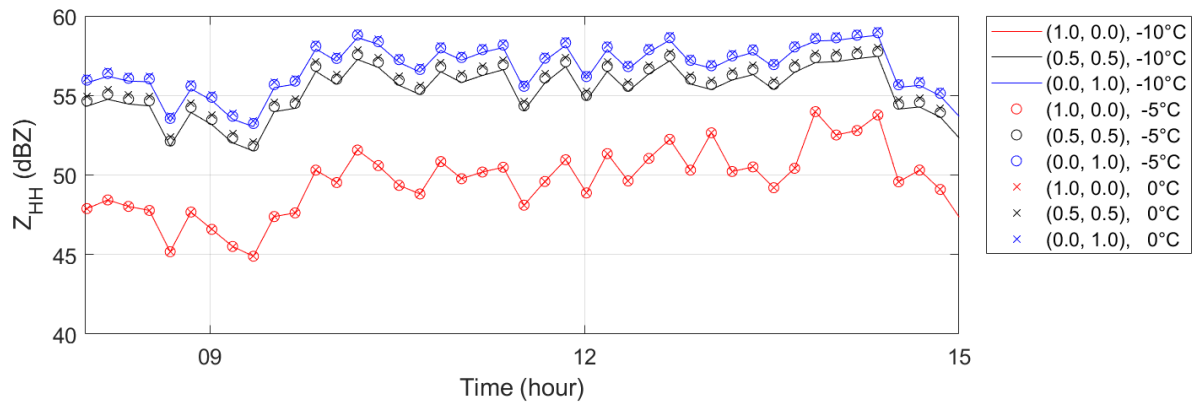




490 **Table 3: The  $V_Z$  criteria of the five sites are determined as the absolute value of the  $V_Z$  mean bias of the sites plus one standard deviation of the bias. The  $V_Z$  mean bias are the average of the  $V_Z$  difference between of MRR measurement and derived density calculation during all events available (Table 1) while the standard deviation of the bias is the standard deviation of the  $V_Z$  difference.**

		YPO	MHS	CPO	BKC	GWU	ALL
$V_Z$	$V_Z$ criteria ( $m s^{-1}$ )	0.94	0.94	0.89	0.84	1.08	nan
	Mean bias ( $m s^{-1}$ )	-0.27	-0.16	-0.12	0.03	0.14	-0.07
	Standard deviation ( $m s^{-1}$ )	0.67	0.78	0.77	0.81	0.94	0.80
SR	Mean bias ( $mm hr^{-1}$ )	-0.14	-0.11	nan	-0.27	-0.19	-0.18
	Correlation coefficient	0.70	0.52		0.74	0.68	nan
	Standard deviation ( $mm hr^{-1}$ )	0.73	1.09		0.85	1.01	0.93

495



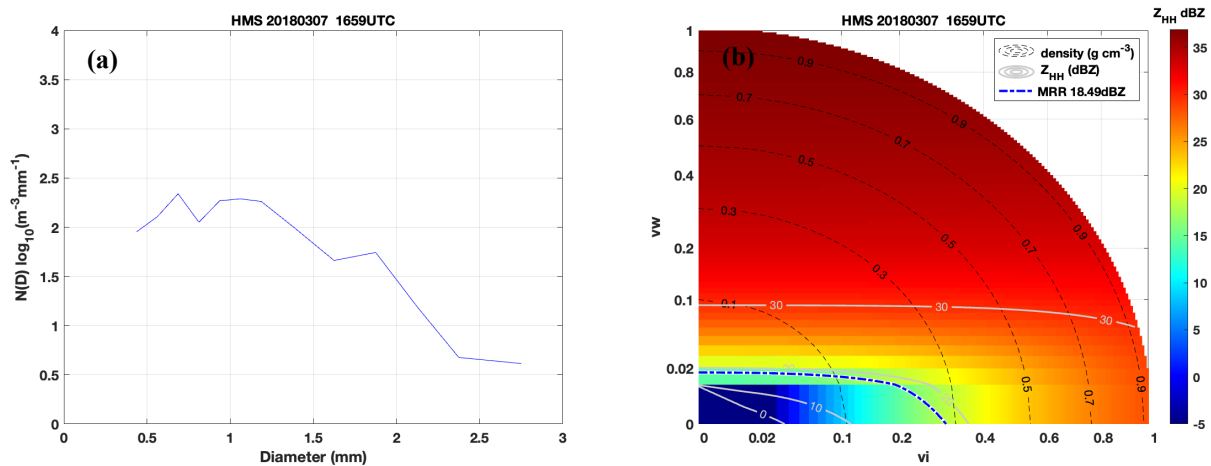
500 **Figure 1: The simulated  $Z_{HH}$  with combinations of the volume ratio of solid ice and liquid water ( $v_i$ ,  $v_w$ ) and temperature is demonstrated by a case from the Parsivel observation of MHMS site on 28 February 2018. The combinations of ( $v_i$ ,  $v_w$ ) were (1.0, 0.0) in red, (0.5, 0.5) in black, and (0.0, 1.0) in blue lines. The temperature values were -10, -5, and 0°C (thick line, circle, and cross marks).**

505

510

515

520

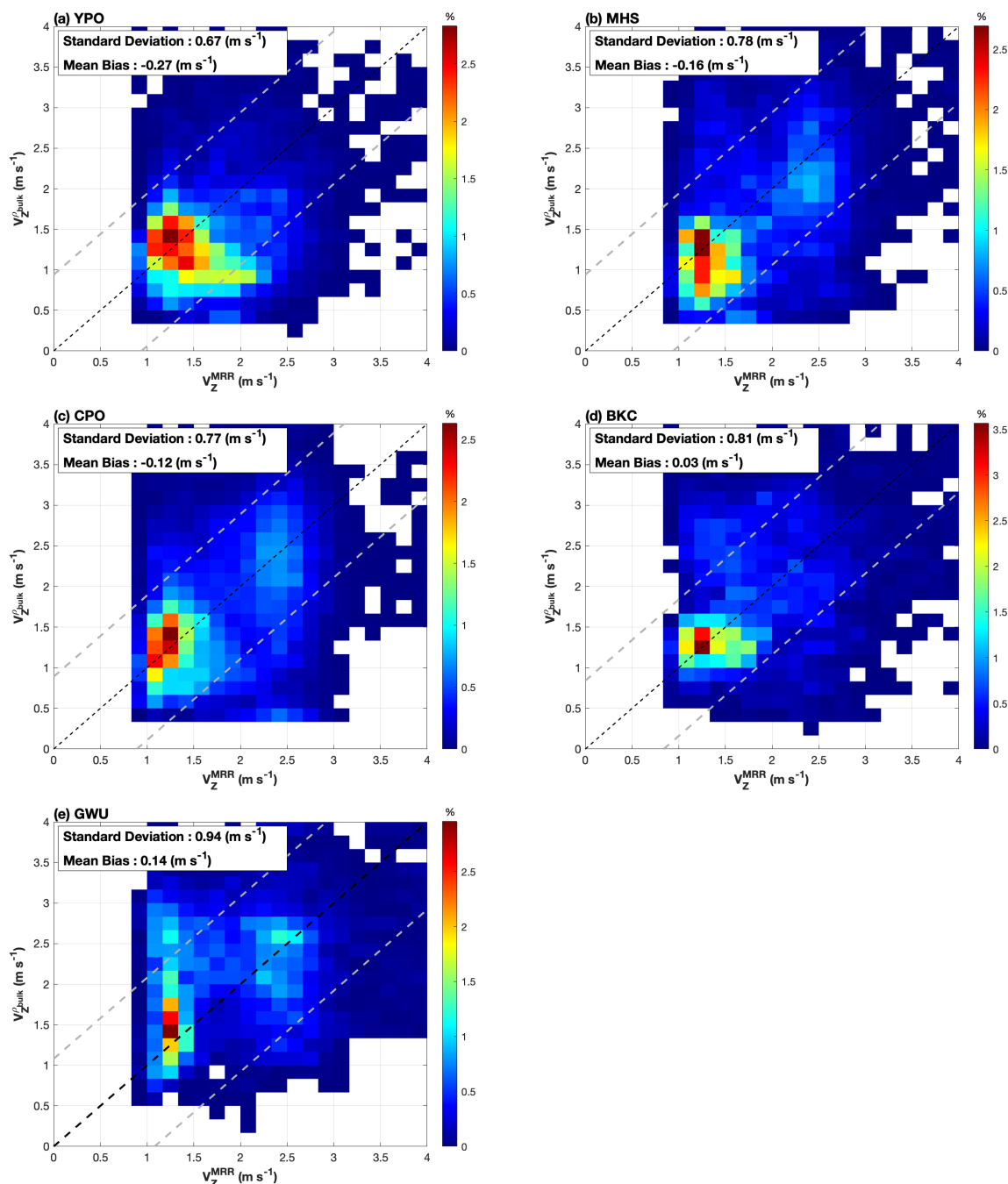


525 **Figure 2: (a) Observed snow size distribution,  $N(D)$ , from the MHS Parsivel site at 1659 UTC on 7 March 2018. (b)  $Z_{HH}$  distribution simulated from the Parsivel DSD. The x- and y-axis are the volume ratio of solid ice ( $v_i$ ) and liquid water ( $v_w$ ), respectively. The shaded color indicates the  $Z_{HH}$  magnitude (dBZ), and the black dashed lines are contours of density ( $\text{g cm}^{-3}$ ). Grey solid lines are contours of  $Z_{HH}$  (dBZ). The  $Z_{HH}$  variation with  $v_w$  is much less than that with  $v_i$  on the contours of  $Z_{HH}$ . The blue dashed-dot line is the value of the collocated MRR measurement of  $Z_{HH}$  (dBZ).**

530

535

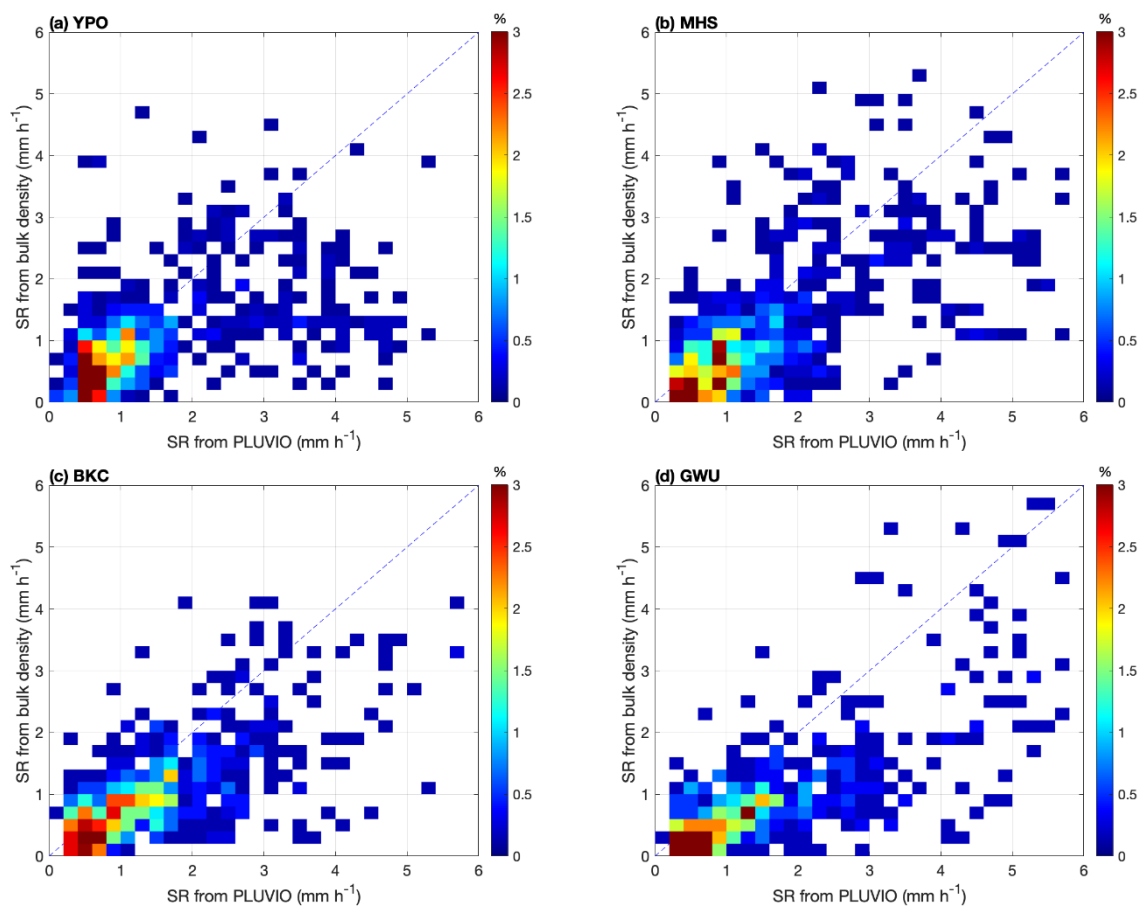
540



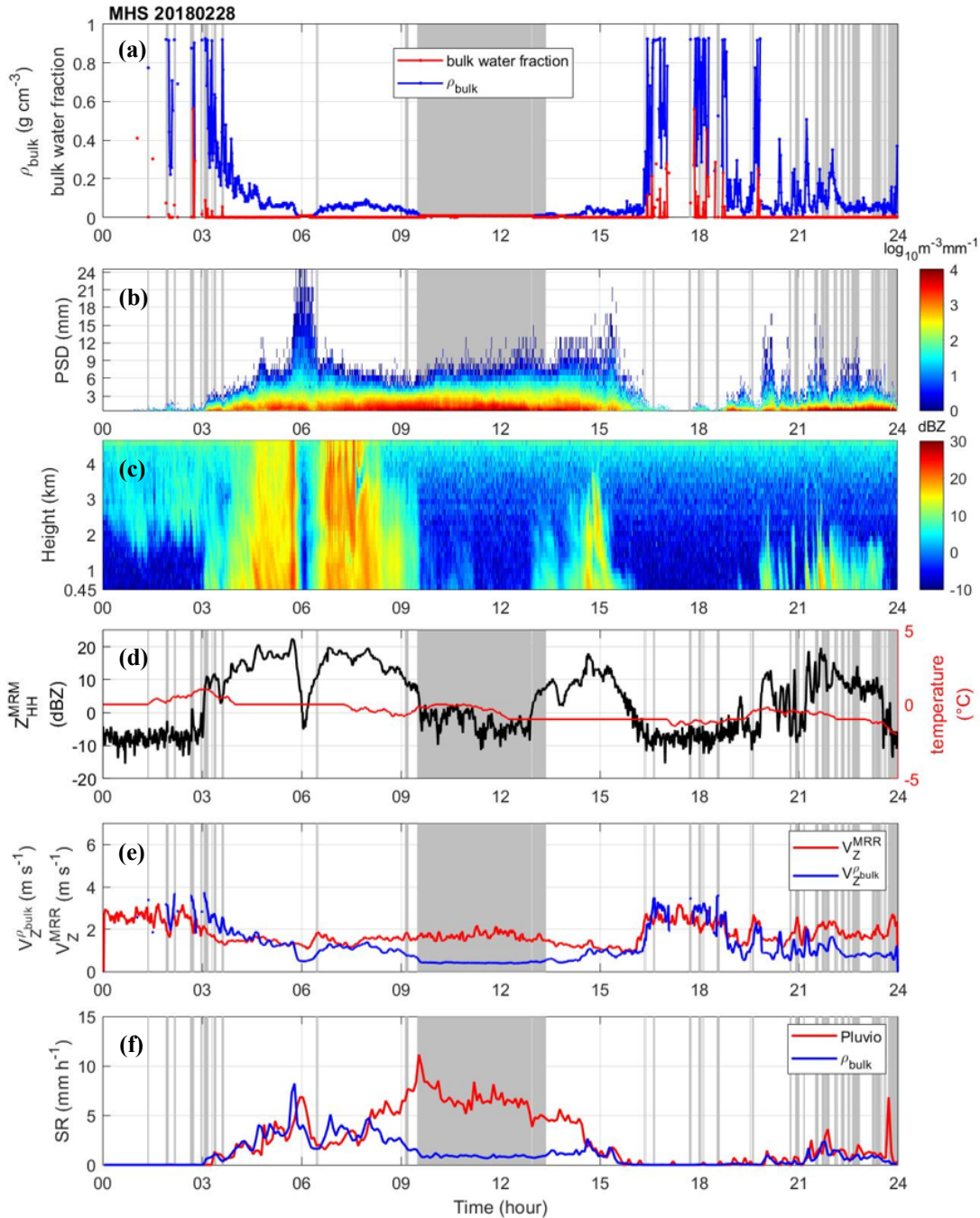
545

Figure 3: The probability density function of  $Z_{HH}$  weighted fall velocity ( $V_Z^{\rho_{bulk}}$ ) calculated from "bulk density" and the MRR measurement ( $V_Z^{MRR}$ ) in (a) MHS, (b) CPO, (c) BKC, (d) GWU, and (e) YPO site. The gray dash lines are the  $V_z$  criteria.

550



555 **Figure 4: Normalized number density function of SR from density-derived and Pluvio observed SR in (a) YPO, (b) MHS, (c) BKC, and (d) GWU site. The data has been V<sub>Z</sub> quality controlled.**

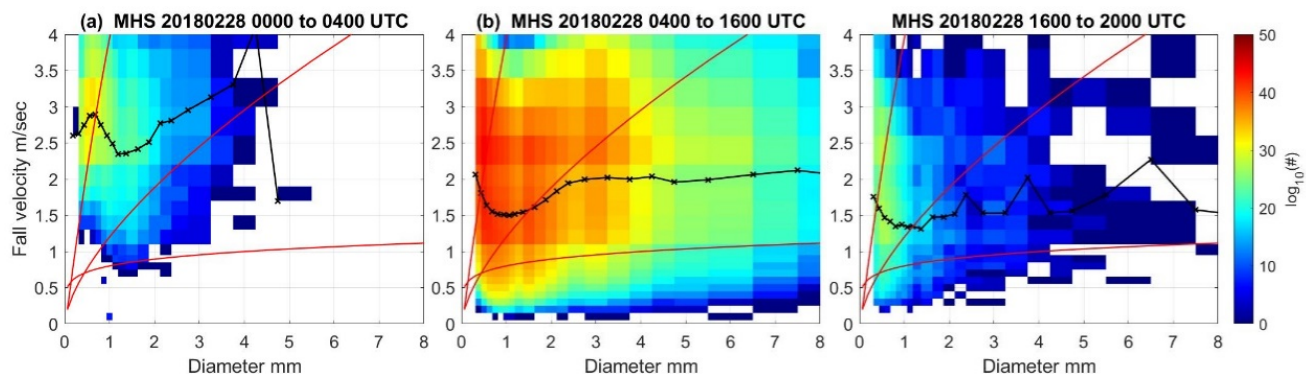


560 **Figure 5:** The data from MHS site on 28 February 2018. (a) Derived bulk density ( $\text{g cm}^{-3}$ , blue line), bulk water fraction (red line). (b) Parsivel PSD in logarithm scale. (c) The vertical profile of  $Z_{\text{HH}}$  from the third layer (0.45 km) to the top (dBZ, shaded area) of MRR. (d) The temperature ( $^{\circ}\text{C}$ , red line) and  $Z_{\text{HH}}$  from third layer. (e) The velocity ( $V_Z^{\text{MRR}}$ ) of MRR measurement (red line) and the  $Z_{\text{HH}}$  weighted velocity ( $V_Z^{\rho_{\text{bulk}}}$ ) calculated from bulk density (blue line). (f) The liquid-equivalent snow-rate (SR) of Pluvio measurement (red line) and bulk density derived SR (blue line). The inadequate retrieval which the  $V_Z$  difference between  $V_Z^{\text{MRR}}$  and  $V_Z^{\rho_{\text{bulk}}}$  greater than the  $V_Z$  criteria (Table 3) of MHS site are indicated by gray area.



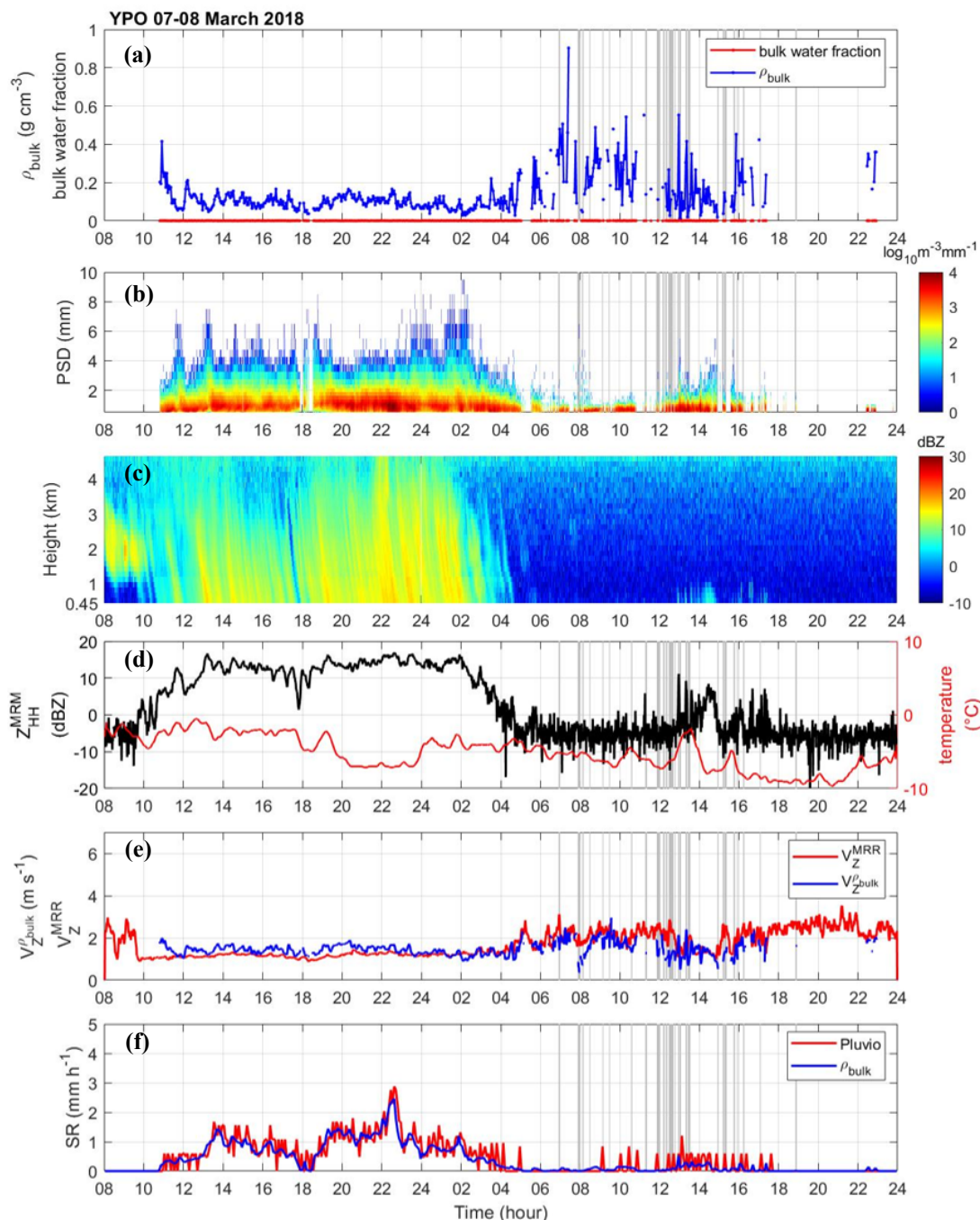


565

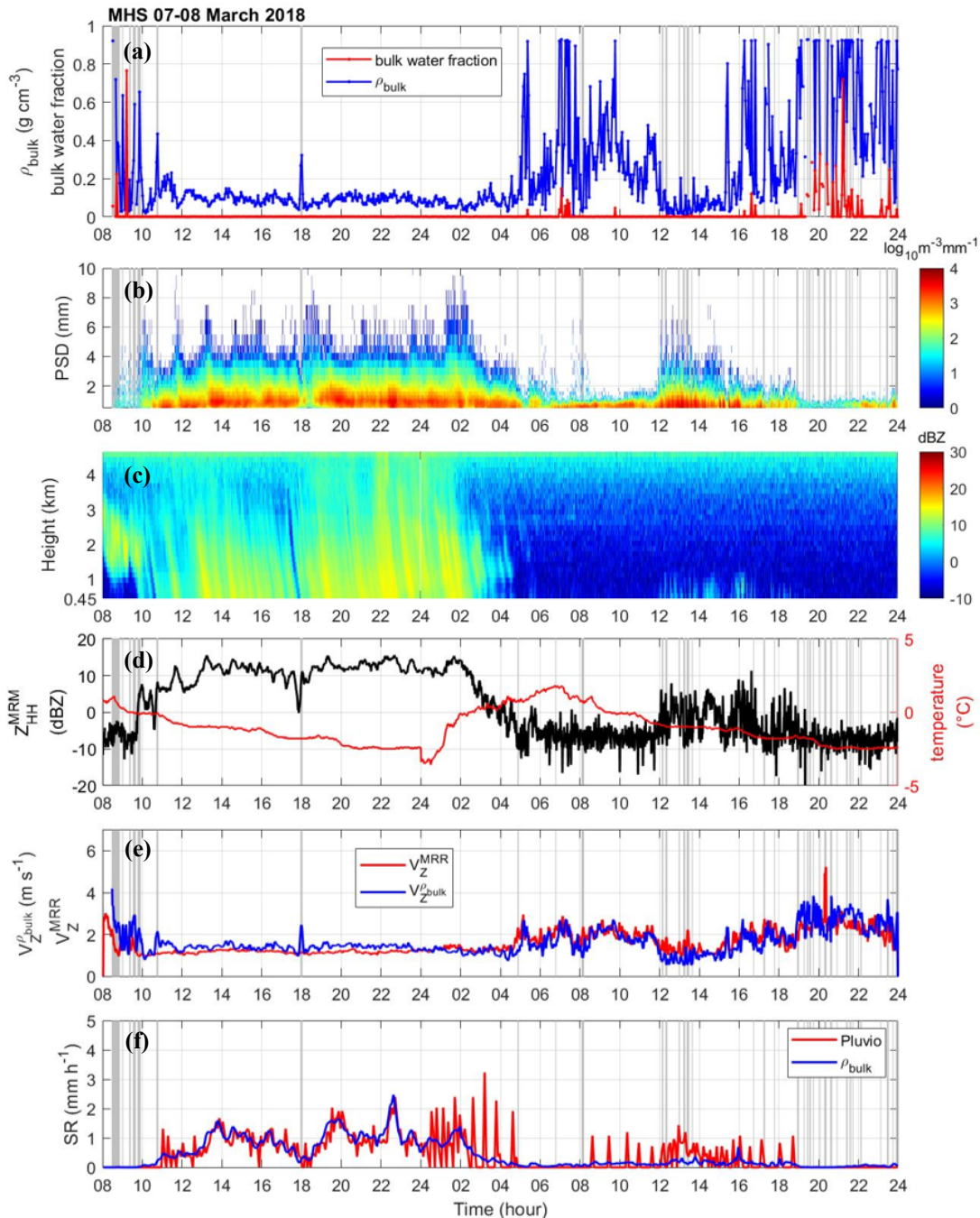


570

**Figure 6:** The number density function of fall velocity and diameter from Parsivel (logarithm scale shown in color-shaded) collected from 28 February 2018. The average of fall velocity in each diameter bin ( $\text{m s}^{-1}$ , black line), relations of fall velocity-diameter of rain, graupel, and dry dendrites (from the upper to lower red line) are derived for (a) 00 to 04 UTC, (b) 04 to 16 UTC, and (c) 16 to 20 UTC in the MHS site. The relation of rain is from Brandes et al. (2002). The relations of graupel and dry dendrites are from Locatelli and Hobbs (1974).



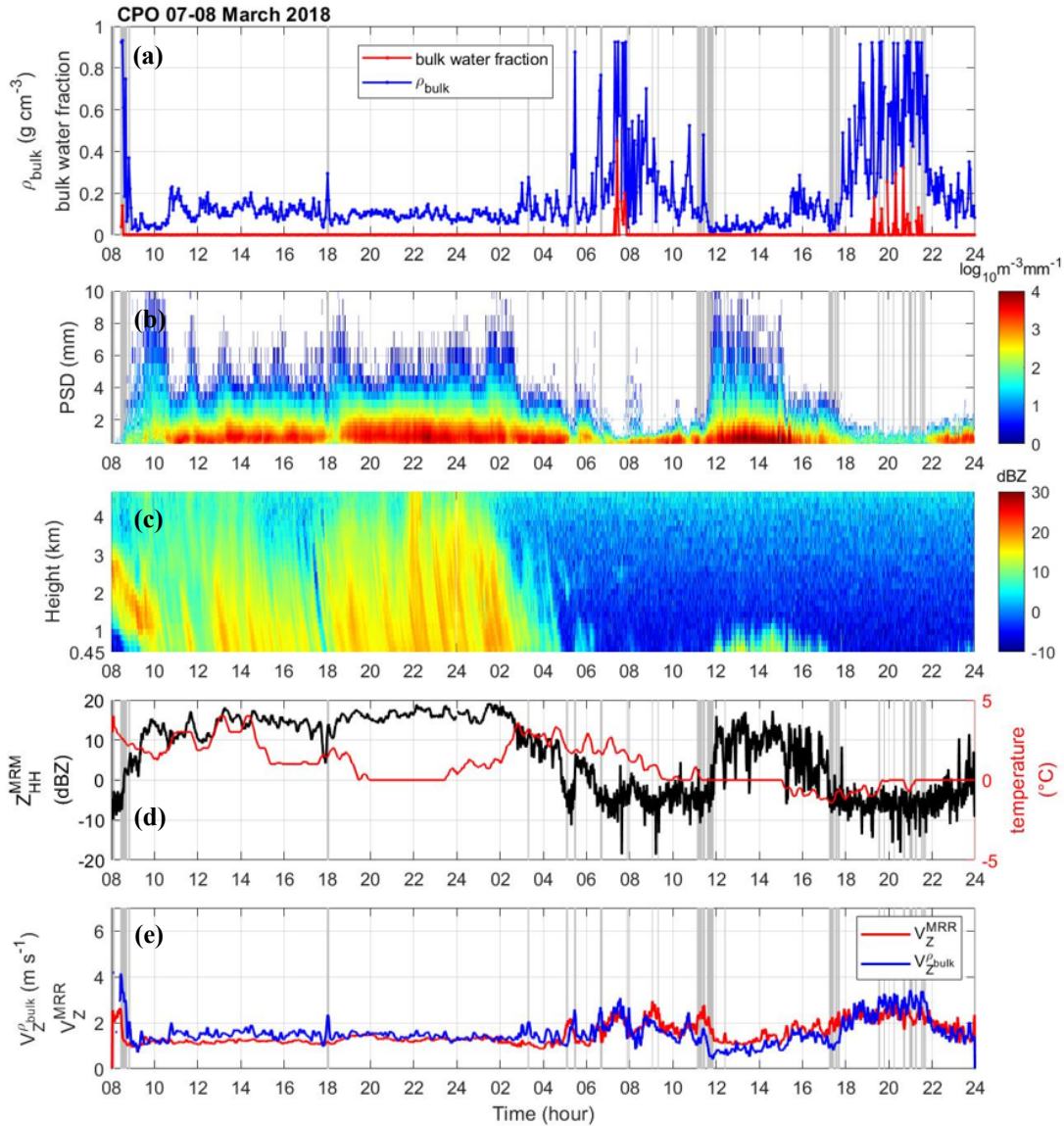
575 **Figure 7: The data from YPO site on 7 March 2018. (a) Derived bulk density ( $g\ cm^{-3}$ , blue line), bulk water fraction (red line). (b) Parsivel PSD in logarithm scale. (c) The vertical profile of  $Z_{HH}$  from the third layer (0.45 km) to the top (dBZ, shaded area) of MRR. (d) The temperature ( $^{\circ}C$ , red line) and  $Z_{HH}$  from third layer. (e) The velocity ( $V_Z^{MRR}$ ) of MRR measurement (red line) and the  $Z_{HH}$  weighted velocity ( $V_Z^{\rho_{bulk}}$ ) calculated from bulk density (blue line). (f) The liquid-equivalent snow-rate (SR) of Pluvio measurement (red line) and bulk density derived SR (blue line). The inadequate retrieval which the  $V_Z$  difference between  $V_Z^{MRR}$  and  $V_Z^{\rho_{bulk}}$  greater than the  $V_Z$  criteria (Table 3) of MHS site are indicated by gray area.**



580

**Figure 8: The data from MHS site on 7 March 2018. (a) Derived bulk density ( $g\ cm^{-3}$ , blue line), bulk water fraction (red line). (b) Parsivel PSD in logarithm scale. (c) The vertical profile of  $Z_{HH}$  from the third layer (0.45 km) to the top (dBZ, shaded area) of MRR. (d) The temperature ( $^{\circ}C$ , red line) and  $Z_{HH}$  from third layer. (e) The velocity ( $V_Z^{MRR}$ ) of MRR measurement (red line) and the  $Z_{HH}$  weighted velocity ( $V_Z^{\rho_{bulk}}$ ) calculated from bulk density (blue line). (f) The liquid-equivalent snow-rate (SR) of Pluvio measurement (red line) and bulk density derived SR (blue line). The inadequate retrieval which the  $V_Z$  difference between  $V_Z^{MRR}$  and  $V_Z^{\rho_{bulk}}$  greater than the  $V_Z$  criteria (Table 3) of MHS site are indicated by gray area.**

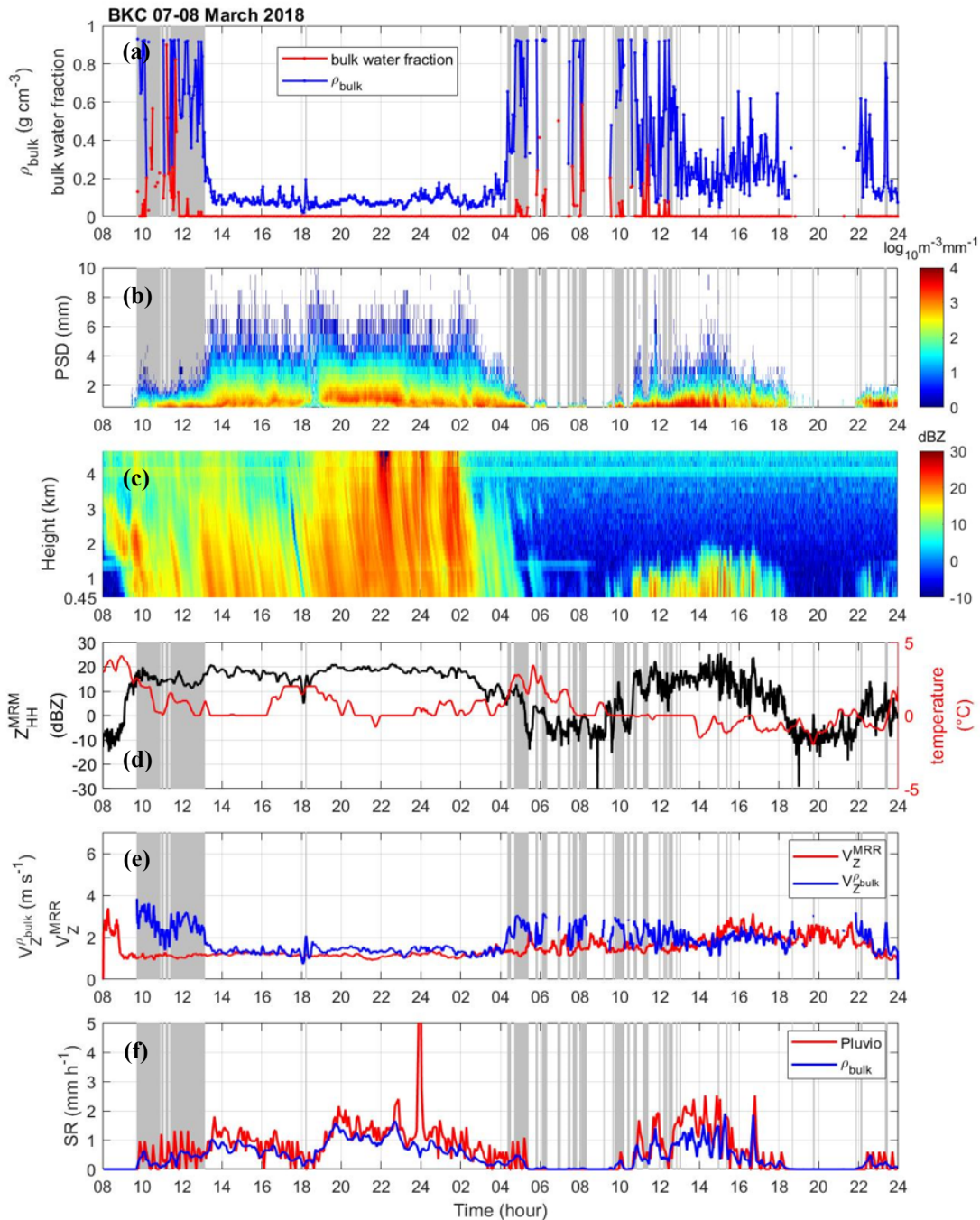
585



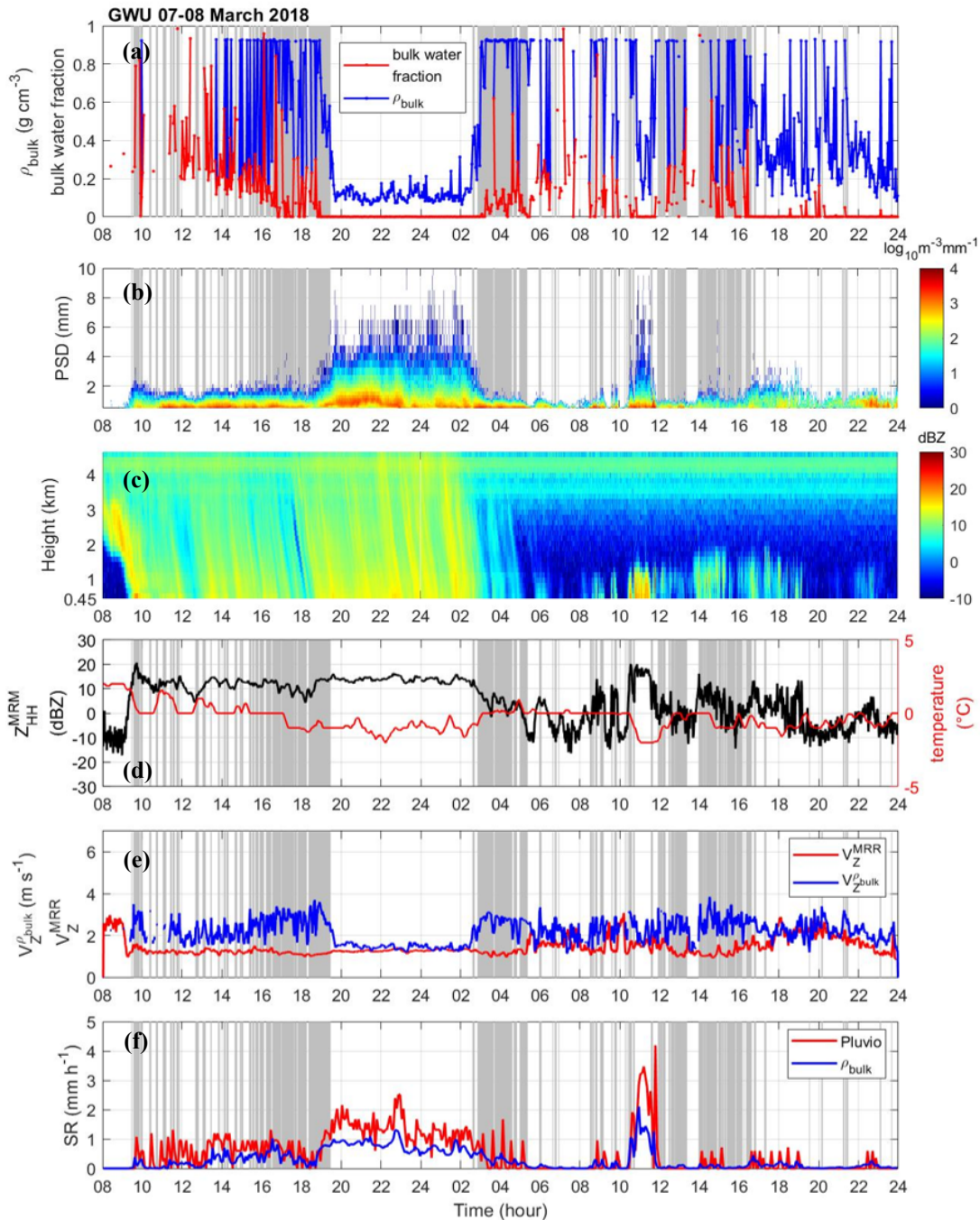
590

**Figure 9:** The data from CPO site on 7 March 2018. (a) Derived bulk density ( $\text{g cm}^{-3}$ , blue line), bulk water fraction (red line). (b) Parsivel PSD in logarithm scale. (c) The vertical profile of  $Z_{\text{HH}}$  from the third layer (0.45 km) to the top (dBZ, shaded area) of MRR. (d) The temperature ( $^{\circ}\text{C}$ , red line) and  $Z_{\text{HH}}$  from third layer. (e) The velocity ( $V_Z^{\text{MRR}}$ ) of MRR measurement (red line) and the  $Z_{\text{HH}}$  weighted velocity ( $V_Z^{\rho_{\text{bulk}}}$ ) calculated from bulk density (blue line). The inadequate retrieval which the  $V_Z$  difference between  $V_Z^{\text{MRR}}$  and  $V_Z^{\rho_{\text{bulk}}}$  greater than the  $V_Z$  criteria (Table 3) of MHS site are indicated by gray area. The Pluvio is not available in CPO site.





595 **Figure 10:** The data from BKC site on 7 March 2018. (a) Derived bulk density ( $\text{g cm}^{-3}$ , blue line), bulk water fraction (red line). (b) Parsivel PSD in logarithm scale. (c) The vertical profile of  $Z_{\text{HH}}$  from the third layer (0.45 km) to the top (dBZ, shaded area) of MRR. (d) The temperature ( $^{\circ}\text{C}$ , red line) and  $Z_{\text{HH}}$  from third layer. (e) The velocity ( $V_Z^{\text{MRR}}$ ) of MRR measurement (red line) and the  $Z_{\text{HH}}$  weighted velocity ( $V_Z^{\rho_{\text{bulk}}}$ ) calculated from bulk density (blue line). (f) The liquid-equivalent snow-rate (SR) of Pluvio measurement (red line) and bulk density derived SR (blue line). The inadequate retrieval which the  $V_Z$  difference between  $V_Z^{\text{MRR}}$  and  $V_Z^{\rho_{\text{bulk}}}$  greater than the  $V_Z$  criteria (Table 3) of MHS site are indicated by gray area.

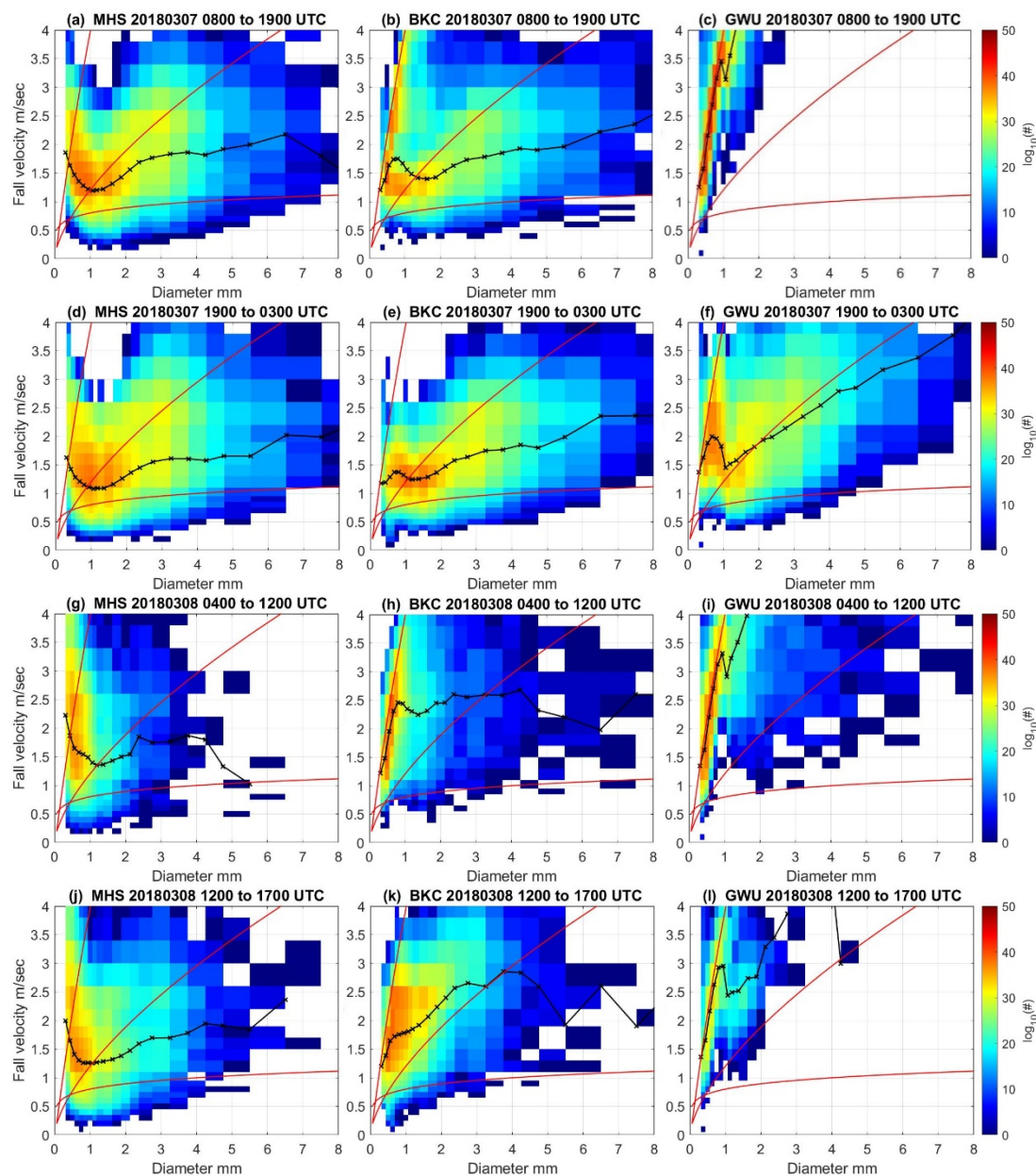


600

**Figure 11:** The data from GWU site on 7 March 2018. (a) Derived bulk density ( $\text{g cm}^{-3}$ , blue line), bulk water fraction (red line). (b) Parsivel PSD in logarithm scale. (c) The vertical profile of  $Z_{\text{HH}}$  from the third layer (0.45 km) to the top (dBZ, shaded area) of MRR. (d) The temperature ( $^{\circ}\text{C}$ , red line) and  $Z_{\text{HH}}$  from third layer. (e) The velocity ( $V_Z^{\text{MRR}}$ ) of MRR measurement (red line) and the  $Z_{\text{HH}}$  weighted velocity ( $V_Z^{\rho_{\text{bulk}}}$ ) calculated from bulk density (blue line). (f) The liquid-equivalent snow-rate (SR) of Pluvio measurement (red line) and bulk density derived SR (blue line). The inadequate retrieval which the  $V_Z$  difference between  $V_Z^{\text{MRR}}$  and  $V_Z^{\rho_{\text{bulk}}}$  greater than the  $V_Z$  criteria (Table 3) of MHS site are indicated by gray area.

605



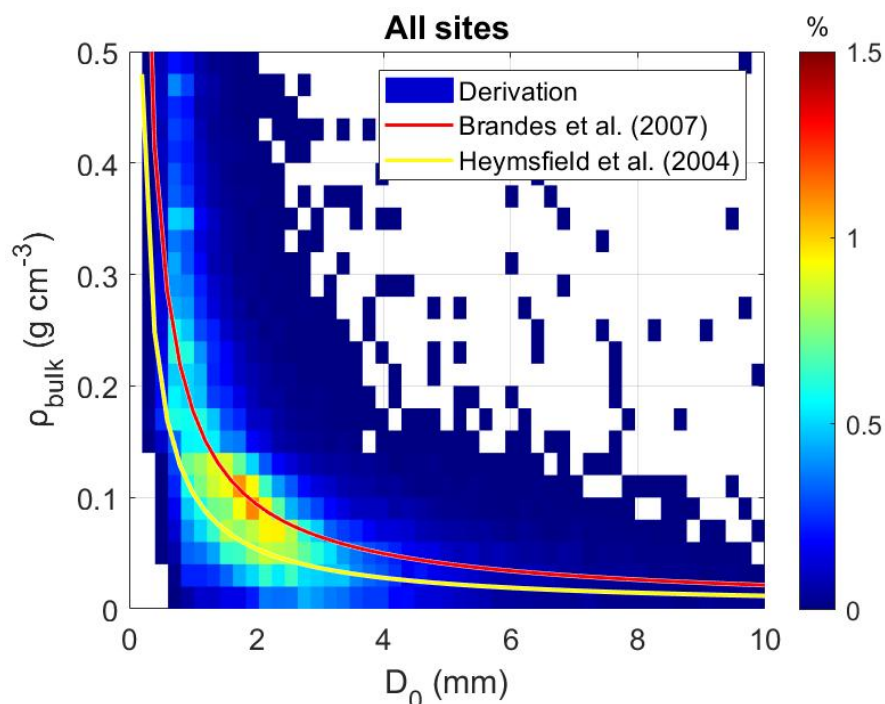


610

Figure 12: The number density function of fall velocity and diameter from Parsivel (logarithm scale shown in color-shaded) from MHS, BKC, and GWU sites collected from 7-8 March 2018. The average of fall velocity in each diameter bin ( $\text{m s}^{-1}$ , black line), relations of fall velocity-diameter of rain, graupel, and dry dendrites (from the upper to lower red line) are derived for (a)~(c) 08-19 UTC on 7 March, (d)~(f) 19 UTC on 7 March to 03 UTC on 8 March, (g)~(i) 04-12 UTC on 8 March, and (j)~(l) 12-17 UTC on 8 March in the MHS, BKC, and GWU sites. The relation of rain is from Brandes et al. (2002). The relations of graupel and dry dendrites are from Locatelli and Hobbs (1974).

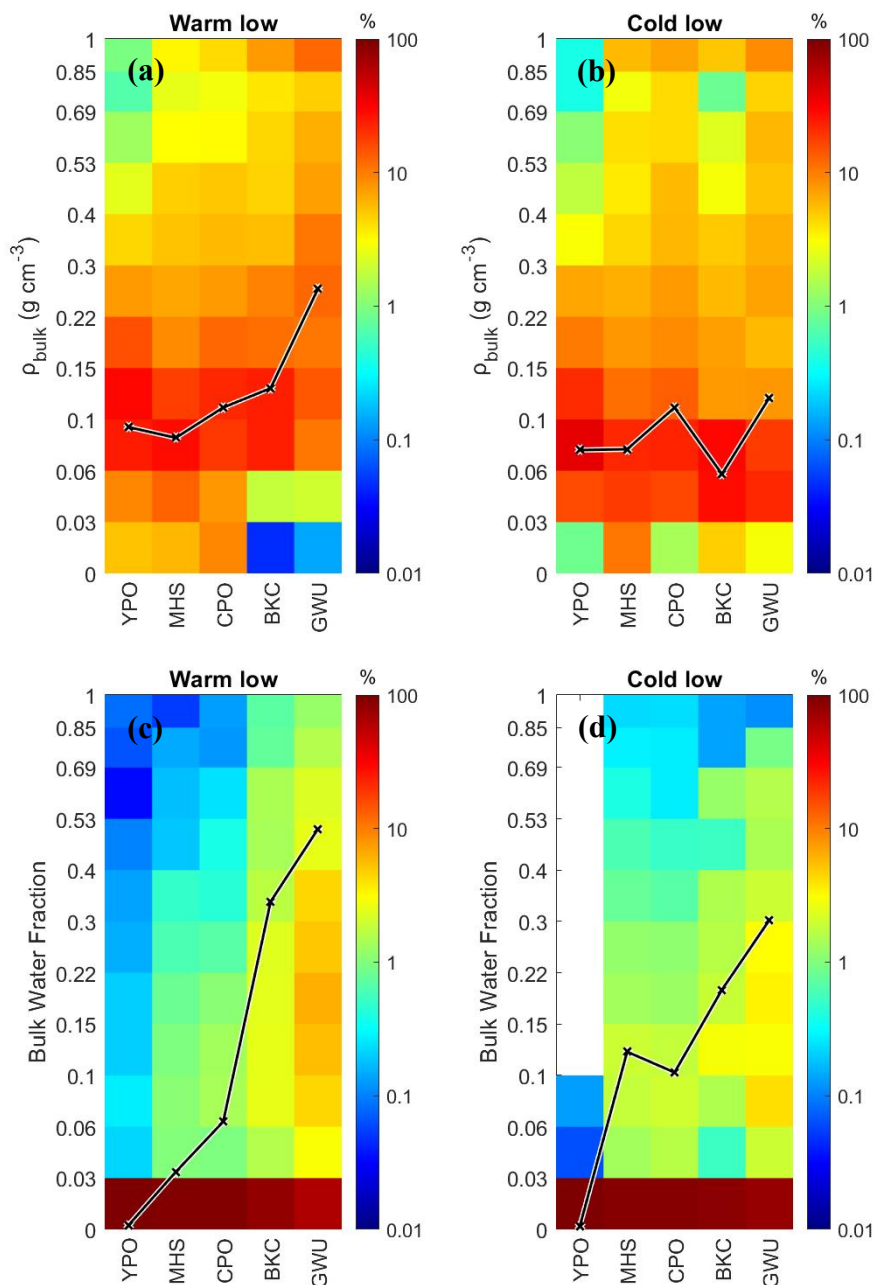
615

620



625 Figure 13: The number density function of retrieved bulk density and observed median-volume diameter ( $D_0$ ) from all sites of entire ICE-POP 2018 and its pre-campaign is shown in shaded. The red and yellow lines represent the  $\rho_{bulk} - D_0$  relation from Brandes et al. (2007) and Heymsfield et al. (2004), respectively.

630



635

640

**Figure 14:** (a) The normalized number density function of retrieved bulk density of each site for warm-low events. The black line indicates the mean bulk density of each site. (b) Same as in (a), but for cold-low events. (c) The normalized number density function of retrieved bulk water fraction of each site for warm-low events. The black line represents the mean values of each site's top 5% bulk water fraction. (d) Same as in (c), but for cold-low events. The normalization is individually applied to every site, ensuring that the total sum of the normalized distribution for each site equals 100%.